small methods
www.small-methods.com

V_4C_3 MXene Immune Profiling and Modulation of T Cell-Dendritic Cell Function and Interaction

Laura Fusco, Arianna Gazzi, Christopher E. Shuck, Marco Orecchioni, Eiman I Ahmed, Linda Giro, Barbara Zavan, Açelya Yilmazer, Klaus Ley, Davide Bedognetti, Yury Gogotsi, and Lucia Gemma Delogu**

Although vanadium-based metallodrugs are recently explored for their effective anti-inflammatory activity, they frequently cause undesired side effects. Among 2D nanomaterials, transition metal carbides (MXenes) have received substantial attention for their promise as biomedical platforms. It is hypothesized that vanadium immune properties can be extended to MXene compounds. Therefore, vanadium carbide MXene (V_4C_3) is synthetized, evaluating its biocompatibility and intrinsic immunomodulatory effects. By combining multiple experimental approaches in vitro and ex vivo on human primary immune cells, MXene effects on hemolysis, apoptosis, necrosis, activation, and cytokine production are investigated. Furthermore, V_4C_3 ability is demonstrated to inhibit T cell-dendritic cell interactions, evaluating the modulation of CD40–CD40 ligand interaction, two key costimulatory molecules for immune activation. The material biocompatibility at the single-cell level on 17 human immune cell subpopulations by single-cell mass cytometry is confirmed. Finally, the molecular mechanism underlying V_4C_3 immune modulation is explored, demonstrating a MXene-mediated downregulation of antigen presentation-associated genes in primary human immune cells. The findings set the basis for further V_4C_3 investigation and application as a negative modulator of the immune response in inflammatory and autoimmune diseases.

1. Introduction

Thanks to their outstanding physicochemical properties, the 2D transition metal carbides/carbonitrides (MXenes)[1,2] are currently studied for biomedical applications ranging from artificial organs,[3] intraocular lenses,[4] and theranostics[5,6] to implantable and epidermal electrodes,[7] and many others.[5,6,8–16] In particular, MXene nanosheets exhibit high photothermal-conversion efficiency and localized surface plasmon resonance effect, expanding the field of photodynamic and photothermal therapy,[17] and a high surface area suitable for drug delivery.[18–20] Notably, the high metallic conductivity of MXenes is accompanied by hydrophilicity,[21,22] a fundamental aspect for biomedical purposes.[23]

We recently explored the immune profile of Nb_4C_3, $Mo_2Ti_2C_3$, and Ta_4C_3 MXenes revealing their ability to interact with a broad range of immune cells.[24] 2D MXenes have also been investigated

L. Fusco, A. Gazzi, L. Giro, L. G. Delogu
ImmuneNano Laboratory
Department of Biomedical Sciences
University of Padua
Padua 35121, Italy
E-mail: luciagemma.delogu@unipd.it

L. Fusco, C. E. Shuck, Y. Gogotsi
A. J. Drexel Nanomaterials Institute and Department of Materials Science and Engineering
Drexel University
Philadelphia, PA 19104, USA
E-mail: yg36@drexel.edu

The ORCID identification number(s) for the author(s) of this article can be found under https://doi.org/10.1002/smtd.202300197

DOI: 10.1002/smtd.202300197

L. Fusco, E. I Ahmed, D. Bedognetti
Translational Medicine Department
Sidra Medicine
Doha Qatar

M. Orecchioni, K. Ley
La Jolla Institute for Immunology
San Diego, CA 92037, USA

B. Zavan
Department of Medical Sciences
University of Ferrara
Ferrara 44121, Italy

B. Zavan
Maria Cecilia Hospital
GVM Care & Research
Ravenna 48033, Italy

A. Yilmazer
Stem Cell Institute
Ankara University
Ankara 06520, Turkey

A. Yilmazer
Department of Biomedical Engineering
Ankara University
Ankara 06830, Turkey

as valuable tool in the fight against viral infections such as COVID-19 for their ability to inhibit the viral replication and modulate the immune response, reducing the production of inflammatory cytokines.[14] Additionally, Ti_3C_2 MXene quantum dots stimulate immune cells to produce anti-inflammatory cytokines and promote tissue regeneration, useful in treating various diseases.[25] MXenes, specifically Ta_4C_3 and Ti_3C_2, have demonstrated significant potential in improving the success rate of organ transplantation and have been employed for in vivo prevention and treatment of transplant vasculopathy thanks to their immunomodulatory effects which reduce the activation of T-lymphocytes and infiltration of immune cells.[15,26] Given these advancements, MXenes hold great promise in the field of immunomodulatory medicine. However, the immunocompatibility and possible immune modulatory effects of the single components of this large family of materials are still unexplored. In particular, despite vanadium-based MXenes are among the most popular types of these materials for their applications in energy storage and batteries,[27–31] there are no studies evaluating their immune impact, and only a few data, limited to V_2C, have been reported so far on their potential in biomedicine as biosensors[32] and reactive oxygen species (ROS) scavengers[33,34] In fact, vanadium-based MXenes have been shown to counteract ROS-mediated inflammatory diseases[33] characterized by the presence of ROS in affected tissues, which can lead to oxidative stress and tissue damage. The materials could relieve ROS-induced damage in vivo, alleviating inflammatory and neurodegenerative diseases thanks to their antioxidant enzyme-mimicking properties.[33] In addition, V_2C enzyme-like activities have been employed against ischemic stroke by alleviating oxidative stress, inhibiting cell apoptosis, and counteracting inflammation.[34]

Expanding our knowledge on the unique properties of these materials is of critical importance for their conscious exploration in biology and medicine. In this view, specific application-oriented immune properties of MXenes[35] may have an important role in nanomaterial-based treatments of several diseases.[36–40]

Recent efforts have demonstrated that vanadium species (^{51} V and ^{50} V) are involved in many immune-driven molecular mechanisms that influence and regulate immune responses.[41,42] Indeed, over the last decades, various vanadium compounds have been studied as anti-inflammatory therapeutic metallodrugs targeting various autoimmune responses[43,44] and cancer.[45–50] However, the administration of these vanadium-based nanomedicines has several adverse effects.[41,51–55] Findings reveal that (III), (IV), and (V) vanadium ions influence the maturation and function of dendritic cells (DCs), thus affecting the immune response of effector lymphocytes.[56] Vanadium also modulates immune CD11c and MHC-II expression in thymic DCs by reducing CD11c surface marker expression.[57] This decrease may lead to T cell dysfunction, including possible negative selection.[57] Furthermore, vanadium can affect activation induced T cell signal induction pathways, resulting in the impairment of immune function after vanadium treatment. This effect was reported to alter CD4+ T helper (Th) cell activation, thereby influencing cellular and humoral immune responses.[58]

Therefore, here we explored vanadium carbide MXene (V_4C_3) as a potentially safer biomedical nanotool to fully take advantage of vanadium properties. We selected the formula V_4C_3 as it is more chemically and environmentally stable than V_2C, due to the larger number of atomic layers in its structure. As a reference material, we also included in our study titanium carbide (Ti_3C_2), the most widely studied MXene in biomedicine.[5,6,13,14,25,59,60] The surface of MXenes after wet chemical etching is terminated with O, OH, and some fluorine, as we previously described,[22,61] and their formulas can be written as $Ti_3C_2T_x$ and $V_4C_3T_x$. We evaluated the impact of these nanomaterials on immune functions in primary human and murine immune cells by combining diverse experimental approaches (**Figure 1**A). In particular, we investigated the impact of $Ti_3C_2T_x$ and $V_4C_3T_x$ on DC functionality. Biocompatibility studies for nanomaterials have primarily focused on their interactions with cells without considering the potential modulation of cell–cell interactions. However, when evaluating the impact of nanomaterials on the immune system, it is important to consider not only their effects on individual immune cells but also how they may affect the interactions between these cells. As part of our research, we investigated how MXenes may affect the interactions between T cells and dendritic cells (DCs). Specifically, we focused on CD40-CD40L interactions, which are essential for antigen presentation and to activate immune responses by promoting the production of cytokines and costimulatory molecules that activate T cells and promote their differentiation.[62] These interactions are crucial for maintaining effective immune responses, and deficiencies in CD40 or CD40L can compromise the immune system's ability to fight off diseases. On the other hand, blocking CD40–CD40L interactions can help limit immune-mediated tissue damage in cases of cancer and autoimmune diseases opening to future applications of MXenes.

To assess the potential immune modulatory effects of MXenes on a wide number of immune subpopulations, we conducted ex vivo experiments at the single-cell level using high-dimensional single-cell mass cytometry by time-of-flight (CyTOF). This technique, based on mass spectrometry to detect metal element-tagged probes according to their mass/charge ratio (m/z), allowed the simultaneous detection of 36 markers with minimal overlap or signal background.[63,64] The impact of MXenes on cell viability and functionality was dissected accordingly on 17 different human immune cell subpopulations and 11 major cytokines. Finally, to have a broad view of the molecular effects of V_4C_3 on $PBMC_S$, the impact at the protein and gene level was assessed by multiplex protein arrays and RNA sequencing (mRNA-seq) since these technologies are able to evaluate the effects on the modulation of a wide number of inflammatory mediators and genes allowing us to investigate the possible mechanisms of action of

D. Bedognetti
Department of Internal Medicine and Medical Specialties
University of Genoa
Genoa 16132, Italy
D. Bedognetti
College of Health and Life Sciences
Hamad Bin Khalifa University
Doha Qatar
L. G. Delogu
New York University Abu Dhabi
Abu Dhabi United Arab Emirates

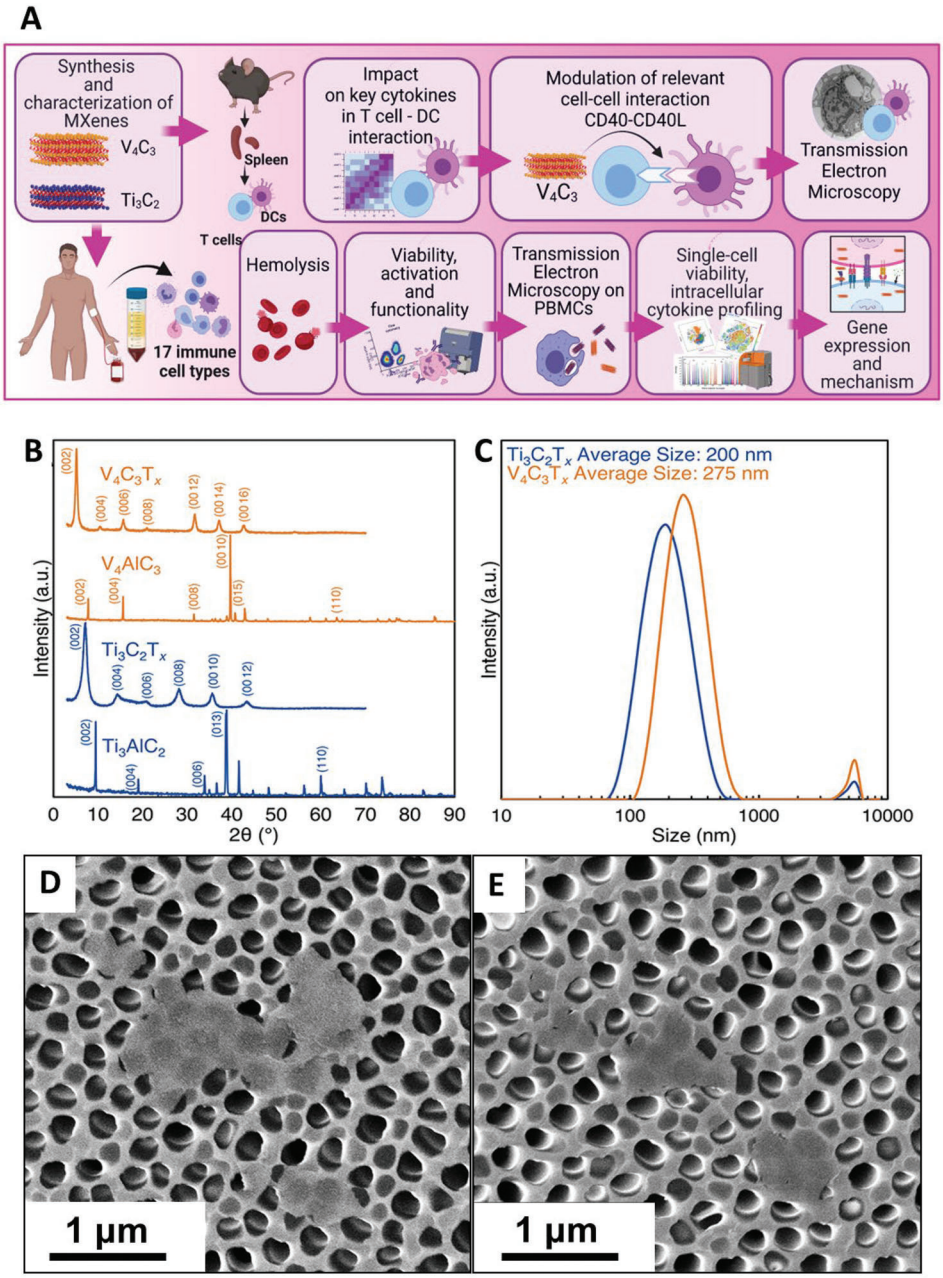

Figure 1. Workflow and characterization of Ti_3C_2 and V_4C_3 MXenes. A) Overview of the workflow. B) X-ray diffraction (XRD) patterns of the MAX phase precursors used for synthesis of MXenes and of vacuum-filtered MXene films. C) Dynamic light scattering (DLS) of Ti_3C_2 and V_4C_3 showing the flake size distributions of the MXenes used. D) Scanning electron microscopy (SEM) images of $Ti_3C_2T_x$ and E) $V_4C_3T_x$ MXenes on a porous anodic aluminum oxide support.

MXenes. We describe the potential mechanism of V_4C_3 as immunomodulatory platform.

2. Results and Discussion

2.1. Ti_3C_2 and V_4C_3 MXenes: Synthesis and Characterization

MXenes were produced by selectively etching Al from MAX phases (details in the Experimental Section). X-ray diffraction (XRD) patterns of the precursor MAX powders (Ti_3AlC_2 and V_4AlC_3) and delaminated MXenes ($Ti_3C_2T_x$ and $V_4C_3T_x$) are shown in Figure 1B. The MAX phases have a *p*63/*mmc* space group, with the (00l) and (110) peaks labeled. For Ti_3AlC_2, the (002) peak is located at 7.14° (9.26 Å); after the etching and the delamination with tetramethylammonium hydroxide (TMAOH), the peak shifts to 5.94° (12.37 Å) for $Ti_3C_2T_x$. Similar behavior is observed for the V_4AlC_3 conversion to $V_4C_3T_x$, confirming the successful removal of the Al layers for all the MXenes

studied. In the MXene XRD patterns, only the (00l) peaks remain, demonstrating the successful etching and delamination process, with no impurities remaining in the MXene colloid. The functional groups passivate the surface of MXenes and make them hydrophilic. MXenes produced by wet chemical synthesis and delamination have negatively charged surfaces with the zeta-potential below −30 mV and can form stable colloidal solutions in water. MXenes with the same nominal chemical formula but produced by other methods may have different surface chemistry (e.g., Cl terminations, adsorbed Li-ions or a different O:F ratio[1,22,65]). MXenes used in this study present oxygen-dominated surface chemistry. Since we did not study the effect of surface chemistry on immune response. T_x is not used in the following manuscript sessions to simplify the sample annotation of the chemical formula.

Dynamic light scattering (DLS) was used to characterize the average flake size in the MXene colloids (Figure 1C). Ti_3C_2 flakes were on average 200 nm, with flakes up to 1 µm in size, while V_4C_3 had an average flake size of 275 nm. Scanning electron microscopy (SEM; Figure 1D,E) analysis was performed to confirm the successful delamination of the MXene flakes. Based on the representative images, the flakes used in this study are proved to be primarily single-layered (≈1 nm in thickness), with sizes corresponding to DLS results.

2.2. Hemocompatibility and Immunocompatibility of V_4C_3 MXene

The physicochemical properties of nanomaterials, their composition, and the starting material used for their production can ultimately influence their biocompatibility. Given that most biomedical applications of nanotools require the systemic injection of nanomaterials into the bloodstream, assessing their hemocompatibility and immunocompatibility is critical. Therefore, we first evaluated the blood compatibility of V_4C_3 and Ti_3C_2. We investigated their hemolytic activity through hemoglobin release after exposure of human red blood cells (RBCs) to 50 µg mL^{-1} of V_4C_3 or Ti_3C_2 (**Figure 2**A and Figure S1A, Supporting Information). We observed no significant release of hemoglobin induced by the materials, demonstrating their hemocompatibility.

In addition, we evaluated the immune compatibility of the materials, a crucial aspect for their translation into the clinic. To this end, we treated human peripheral blood mononuclear cells (PBMCs) with increasing concentrations (25, 50, and 100 µg mL^{-1}) of V_4C_3 or Ti_3C_2 for 24 h, selecting this incubation time based on previous studies with other nanomaterials on immune cells.[14,66–77] We used EtOH as a positive control. Subsequently, we stained cells with Fixable Viability Staining 780 and analyzed the effect of material exposure by flow cytometry, observing no reduction of PBMC viability (Figure S1B, Supporting Information).

We selected the intermediate concentration of 50 µg mL^{-1} for the following experiments. As displayed in Figure 2B, representing apoptotic and necrotic cells stained with Annexin V, we observed no significant toxic effects induced by the materials on total PBMCs. Even after gating T cells and monocytes, we found no sign of apoptosis or necrosis in these two major immune cell subpopulations (Figure S1C–H, Supporting Information).

In addition, we confirmed the biocompatibility of MXenes on four well-known cell lines broadly used as models for immune toxicity testing in vitro. To this end, we treated K-562 (natural killer cells), JY (B cells), Jurkat (T cells), and THP-1 cells (monocytes) with 50 µg mL^{-1} of V_4C_3 or Ti_3C_2 for 24 h. After treatment, we stained cells with Fixable Viability Staining Zombie NIR and analyzed the effect of material exposure by flow cytometry, observing no reduction of cell viability (Figures S2 and S3, Supporting Information).

Overall, the obtained results show that V_4C_3 and Ti_3C_2 do not cause overt cytotoxic effects. These observations align with published studies addressing the biocompatibility of other members of the MXene family.[5,6,8,14,78]

Once established the biocompatibility of V_4C_3 and Ti_3C_2 with immune cells, we selected 24-h exposure condition as an appropriate time point to evaluate the impact of the selected 2D materials on PBMC functionality in terms of modulation of activation markers, cytokine release, and gene expression. Initially, we assessed V_4C_3 and Ti_3C_2 effects on the expression of two well-known activation markers, namely CD69 and CD25. The former is rapidly upregulated by lymphocytes and across myeloid cells as a consequence of either antigen receptor triggering or innate immune activation, while the latter is constitutively expressed by regulatory T cells but also upregulated by conventional T cells and monocytes upon stimulation. To evaluate the effects of MXenes on these markers, we treated PBMCs with 50 µg mL^{-1} of V_4C_3 or Ti_3C_2 for 24 h and analyzed the cells by flow cytometry. We added lipopolysaccharide (LPS) as a positive control. Interestingly, while Ti_3C_2 caused only a slight but statistically significant reduction of cell surface CD69 expression, V_4C_3 induced a significant decrease of both the activation markers (Figure 2C), suggesting a potential downregulation of immune cell functionality induced in particular by the vanadium-based MXene.

Next, we assessed MXene impact on the production of interleukin (IL)-6, tumor necrosis factor (TNF)-α, and interferon (IFN)-γ, three key proinflammatory cytokines often dysregulated in immunological disorders.[79] We observed no significant increase of the selected inflammatory mediators induced by the exposure of immune cells to V_4C_3 and Ti_3C_2 (Figure 2D and Figure S4, Supporting Information), confirming that these materials do not lead to immune activation, as instead reported for other 2D materials (e.g., graphene).[5,6,80–83]

To further explore the impact of MXenes on immune functions, we evaluated the ability of the materials to counteract the modulation of cytokine production and gene expression induced by LPS priming. To this end, we treated PBMCs with 50 µg mL^{-1} of Ti_3C_2 or V_4C_3 for 24 h with or without LPS priming. The modulation of the production of IL-6 and TNFα was evaluated at the protein and gene level. The obtained results indicate that V_4C_3 strongly decreased the LPS-induced release of IL-6 and TNF-α (Figure 2E) in cell supernatants, while IFN-γ was undetectable (data not shown). This effect was confirmed by gene expression analysis (Figure S4B, Supporting Information). Taken together, these data indicate that V_4C_3 can inhibit immune activation without affecting cell viability.

To evaluate whether the ability of V_4C_3 to negatively modulate the immune cell response was linked to physical interactions with the target cells and internalization of the materials itself, we performed transmission electron microscopy (TEM) analysis

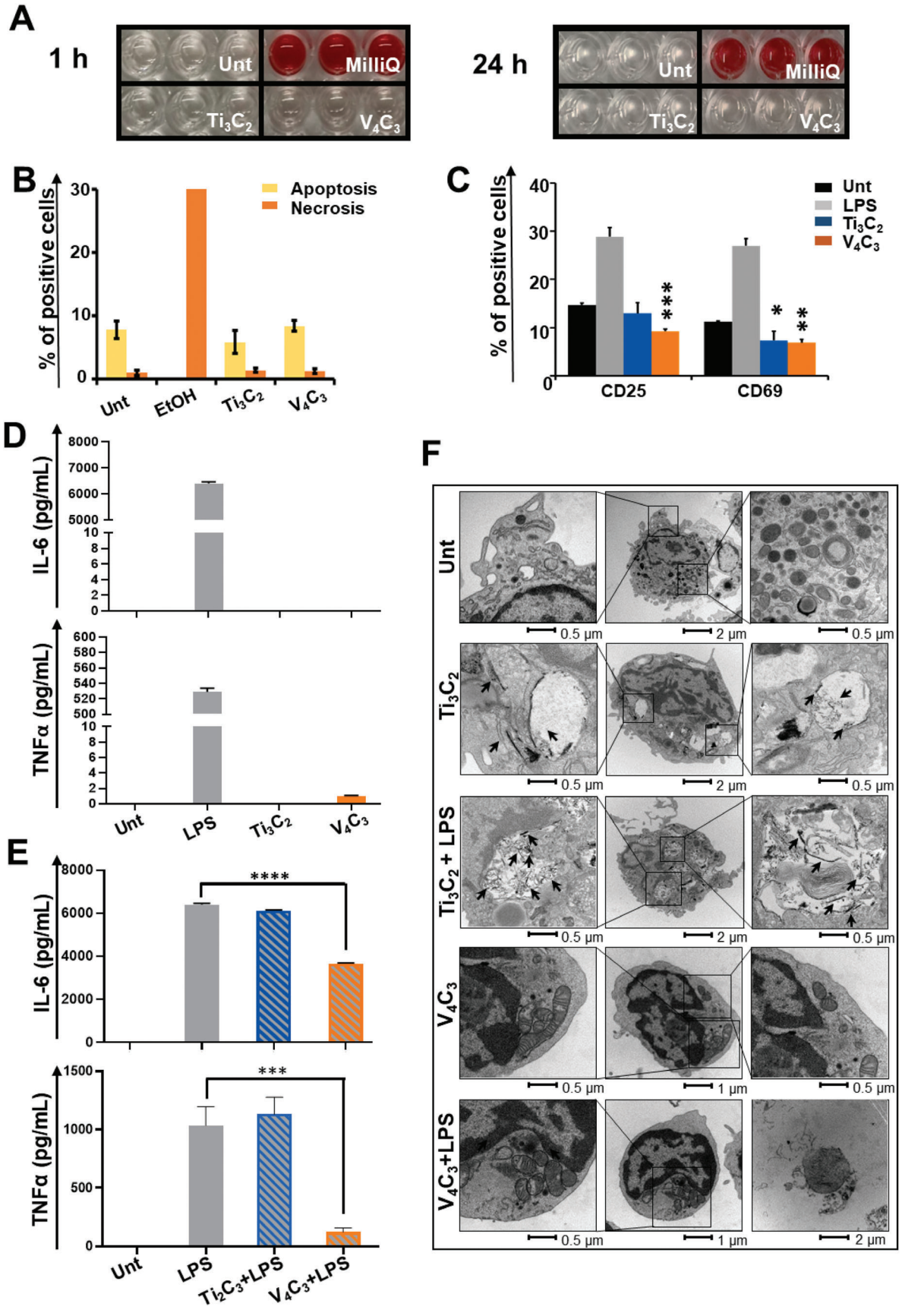

on PBMCs with or without LPS priming to identify cellular localization and possible uptake of the materials (Figure 2F). Of the two materials tested, only Ti_3C_2 was internalized by PBMCs after 24-h incubation, while V_4C_3 was not present in any subcellular compartments. No significant difference in permeability and uptake was observed between MXene-treated samples with or without LPS priming. Since evidence in the literature demonstrated that internalization is closely linked to the chemistry of the material,[84–86] we can speculate on a correlation between internalization and the chemistry of MXenes, as the presence of vanadium may counteract the phagocytic activity of the cells toward V_4C_3.

These results indicate that the immunomodulatory activity shown by V_4C_3 is not dependent on cellular uptake, suggesting that interactions between the material itself and components of the plasma membrane are potentially sufficient to induce the observed biological effects.

2.3. V_4C_3 Interactions on Dendritic Cells and $CD4^+$ T Cells

Having observed in the previous experiments a downmodulation of innate immune cells activation mediated by V_4C_3, we investigated the effect of the nanomaterials on the activation of naïve T cells by DCs—a crucial event in the initiation of the adaptive immune response, relying on the antigen-driven interaction between these two cell types. We first isolated T cells and DCs from C57BL/6J mice and evaluated the ability of the materials to counteract the modulation of TNFα and IL-6 induced by LPS priming in terms of protein release and gene expression. To this end, DCs and T cells in coculture or DCs alone were incubated with 50 μg mL^{-1} of Ti_3C_2 or V_4C_3 for 24 h (**Figure 3**). We observed that V_4C_3 significantly reduced TNFα and IL-6 cytokine release and gene expression in DCs and T cells in coculture and after treatment of DCs alone (Figure 3A,B). Together with the gene expression on total PBMCs, this effect confirms the negative modulation of the innate immune response (Figure S4B, Supporting Information).

To uncover the possible effects of nanomaterials in modulating this process, we measured the interactions between DCs and T cells by tracking CD40–CD40 ligand (CD40L) interactions, a fundamental costimulatory axis in the context of antigen presentation and T cell activation (Figure 3C–G). To this aim, we cocultured wild-type DCs and $CD4^+$ T cells specific for an epitope derived from chicken Ovalbumin ($OVA_{323–339}$, also called OT-II peptide, in the present study called OVA) in the presence or in the absence of OVA (9.25 μg mL^{-1}) and LPS (10 μg mL^{-1}) for 24 h to allow the process of antigen presentation with or without MXenes. CD40 and CD40L surface expression was evaluated by flow cytometry. As expected, CD40L was upregulated by $CD4^+$ T cells upon antigen encounter, but this upregulation was completely abrogated when cells were treated with V_4C_3, and only mildly affected by Ti_3C_2 exposure (Figure 3C–E). Measuring the expression of CD40 on DCs, we detected CD40 upregulation upon LPS treatment and cognate interaction with $CD4^+$ T cells in untreated cells, while no upregulation is present in V_4C_3-treated cultures. We also noticed that upon Ti_3C_2 treatment, the baseline level of CD40 expression is lower than in untreated DCs; however, DCs maintained the ability to upregulate CD40 when stimulated (Figure 3F,G).

Collectively, this data indicates that V_4C_3 significantly modulates the upregulation of CD40 and CD40L, two key costimulatory molecules for immune cell activation. These findings suggest the ability of V_4C_3 to modulate the costimulatory axis in the context of antigen presentation and T cell activation, which was not found for the diverse spectrum of vanadium compounds tested in the literature as anti-inflammatory therapeutic metallodrugs targeting various diseases. In fact, the effect of other vanadium metallodrugs was limited to effector lymphocytes, without affecting the function of DCs.[56]

Subsequently, to evaluate also in murine immune cells whether the immunomodulation induced by the materials was independent from their cellular internalization, we performed TEM analysis upon MXene treatment in primary murine DCs and $CD4^+$ T cells (**Figure 4**). For this purpose, DCs and $CD4^+$ T cells, isolated from C57BL6 mouse spleens, were separately incubated with Ti_3C_2 or V_4C_3 (50 μg mL^{-1}) for 24 h. Consistently with what observed for human PBMCs, V_4C_3 was not taken up by either DCs or $CD4^+$ T cells, while Ti_3C_2 was clearly present in vacuolar structures inside DCs but not in $CD4^+$ T cells (Figure 4).

Overall, the results suggest that V_4C_3 internalization is not necessary to induce the observed immunomodulation of these cell populations.

2.4. V_4C_3 Impact on 17 Human Primary Immune Cell Types

Following our nanoimmunity-by-design concept, a comprehensive view of nanomaterial immune activity can be gained only by studying their potential action in the presence of the complex pool of PBMCs.[35] Therefore, after evaluating V_4C_3 activity toward T cells and DCs in a separate environment, we explored the effects on total PBMCs. To this end, PBMCs were treated with 50 μg mL^{-1} of Ti_3C_2 or V_4C_3 for 24 h and analyzed by single-cell mass cytometry by time-of-flight (CyTOF), to

Figure 2. Effects of MXenes on blood, viability, and function of PBMCs and cell uptake. A) Hemolysis assay performed on human red blood cells (RBCs). RBCs were treated with 50 μg mL^{-1} of Ti_3C_2 or V_4C_3 for 1 and 24 h. MilliQ water was used as a positive control to induce cell lysis. Figure shows pictures of RBCs treated with the nanomaterials. The red color of the solution is due to the release of hemoglobin from lysed RBCs (see Figure S1A in the Supporting Information for absorbance values). B) PBMCs were treated with 50 μg mL^{-1} of V_4C_3 or Ti_3C_2 for 24 h, stained with Annexin V and Fixable Viability Staining 780 and analyzed by flow cytometry. Both, apoptotic and necrotic cells, were expressed as percentage of total cell number. C) Immune cell activation marker staining analysis by flow cytometry. Cells were treated with 50 μg mL^{-1} of Ti_3C_2 or V_4C_3, for 24 h or left untreated (Unt). LPS (2 μg mL^{-1}) was used as a positive control. PBMCs were stained with CD25-PE and CD69-PE-Cy7. D,E) Evaluation of cytokine concentration in supernatants of PBMCs. Cells were treated with 50 μg mL^{-1} of Ti_3C_2 or V_4C_3 for 24 h with and without LPS (2 μg mL^{-1}) priming. Concentration of IL-6, and TNFα was determined. F) Representative TEM images of Ti_3C_2 and V_4C_3 interactions with PBMCs after MXene treatment (50 μg mL^{-1} for 24 h). Arrows in higher magnification micrographs indicate internalized MXenes. As shown in panel, the representative images depict large aggregation and giant vacuoles inside the cells. Scale bars: 2, 1, and 0.5 μm. Data are presented as mean ± S.D. of at least three independent samples. Statistical differences: $*p < 0.05$, $**p < 0.01$, $***p < 0.001$, $****p < 0.0001$ (One-way ANOVA and Tukey's multiple comparison test).

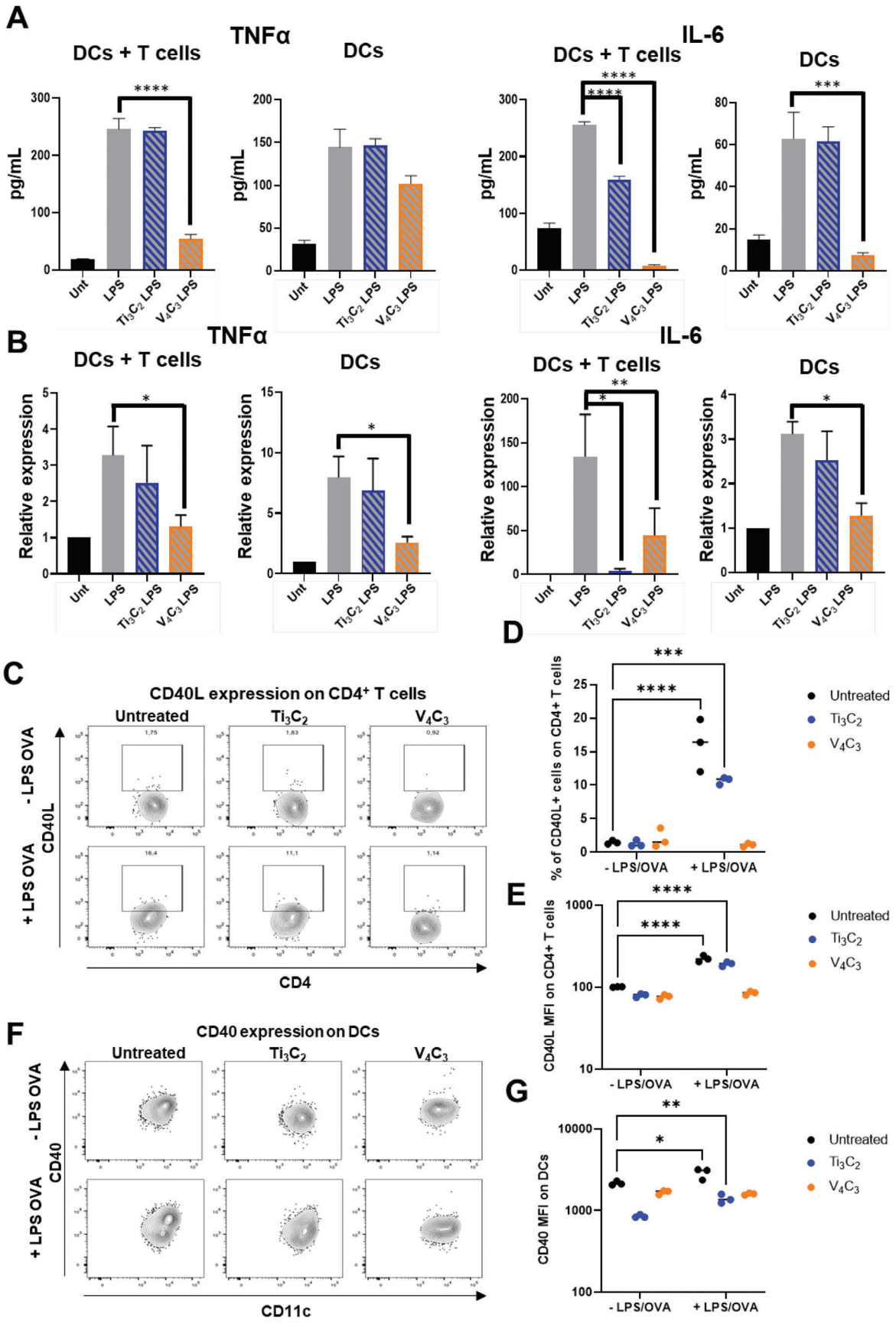

simultaneously analyze 30 markers discriminating 17 immune subpopulations: naïve (naïve Th cells), effector (effector Th cells), memory (memory Th cells), and activated T helper Cells (activated Th. cells), naïve (naïve CT cells), effector (effector CT cells), memory (memory CT cells), and activated cytotoxic T cells (activated CT. cells), classical monocytes (C. monocytes), intermediate monocytes (int. monocytes), nonclassical monocytes (NC. monocytes), myeloid dendritic cells (mDCs), plasmacytoid dendritic cells (pDCs), natural killer cells (NKs), B naive (naïve B cells), B memory (memory B cells) plasma B (plasma B cells), according to the gating strategy reported in Figure S5 (Supporting Information). We used ethanol (EtOH) as a cell death positive control. Computational T-distributed Stochastic Neighbor Embedding (tSNE) analysis was then performed.[66,87] **Figure 5**A reports all the human primary immune subpopulations detected. Figure 5B shows cell viability analysis reported as t-SNE plots and heatmaps for all the selected subpopulations. Ti_3C_2 and V_4C_3 induced no impairment of cell viability on the

Figure 3. V_4C_3 impact on T cells and DCs interaction: cytokines and CD40/CD40L axis. $CD4^+$ T cells and DCs were isolated from C57BL/6J mice and DCs were treated with 50 µg mL^{-1} of Ti_3C_2 or V_4C_3 for 24 h individually or in coculture with T cells (1:1). A) Supernatants were collected to assess TNF-α and IL-6 release. B) The relative gene expression was evaluated by RT-PCR. C) Contour plot representing CD40L expression as measured by flow cytometry in CD4+ T cells. D) Percentage of $CD40L^+$ cells on total $CD4^+$ T cells. E) Mean fluorescence intensity (MFI) of CD40L signal on total $CD4^+$ T cells. F) Countur plot representing CD40 expression as measured by flow cytometry in DCs. G) Mean fluorescence intensity of CD40 signal on total DCs. Data are presented as mean ± S.D. of three independent samples. Statistical differences: $*p < 0.05$, $**p < 0.01$, $***p < 0.001$, $****p < 0.0001$ (One-way ANOVA and Tukey's multiple comparison test).

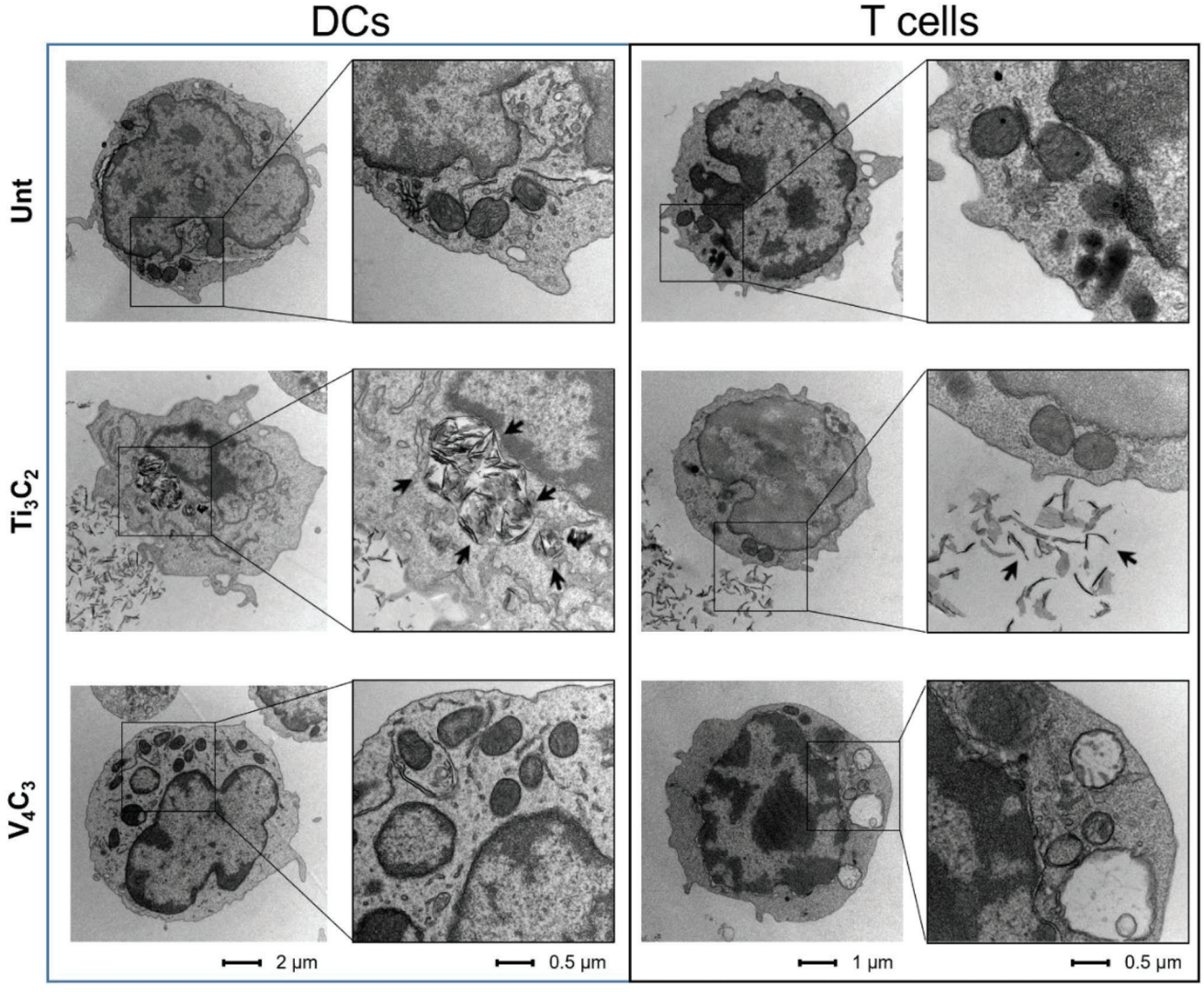

Figure 4. MXene uptake by murine DCs and $CD4^+$ T cells. Representative TEM images of Ti_3C_2 and V_4C_3 interactions with murine DCs and $CD4^+$ T cells after treatment with 50 µg mL^{-1} of Ti_3C_2 or V_4C_3 for 24 h. Arrows in higher magnification micrographs indicate internalized Ti_3C_2 and V_4C_3. As shown in the panel, the representative images depict large aggregations and giant vacuoles inside the cells. Scale bars: 2, 1, and 0.5 µm.

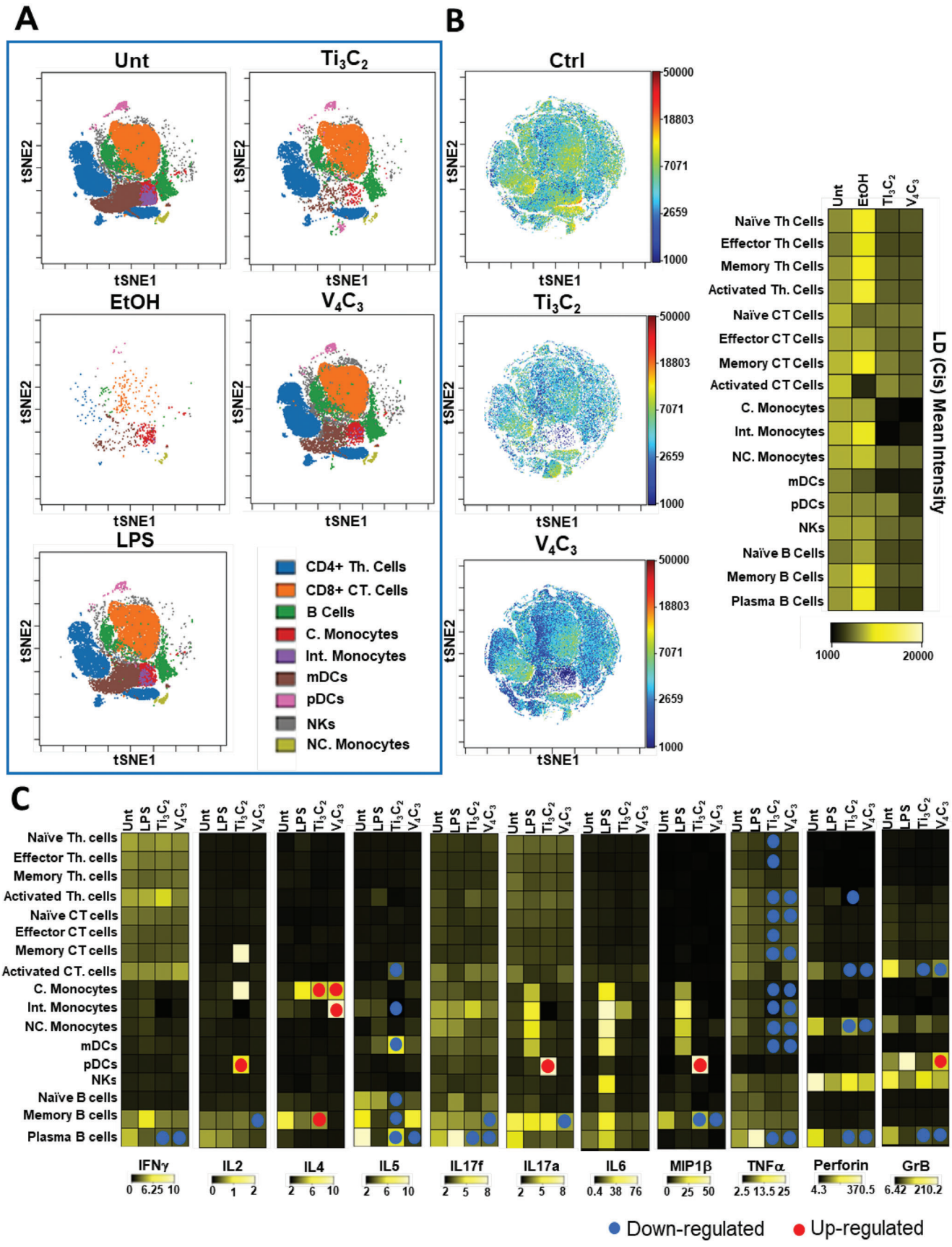

distinct immune cell subpopulations (Figure 5B), confirming the biocompatibility of the materials observed in total PBMCs by flow cytometry (Figure S1B, Supporting Information).

We then evaluated the functional effects of MXenes on human PBMC subpopulations assessing the production of 11 cytokines (including IL-2, IL-4, IL-5, IL-6, TNF-α, IL-17a, IL-17f, and IFN-γ) by CyTOF (Figure 5C). The heatmap in Figure 5C displays the median expression values of all cytokines with respect to each immune subpopulation. The obtained results confirmed the overall downregulatory effects of MXenes, particularly of V_4C_3. TNF-α levels were significantly reduced in all immune subpopulations, except for activated cytotoxic T cell, pDCs, and B cell subsets. The decrease in TNF-α levels in all monocyte subpopulations further supported an anti-inflammatory effect of V_4C_3. Furthermore, MXenes induced an overall downregulation of perforin and granzyme B—proteins that together mediate the apoptosis of target cells after exposure to pro-inflammatory stimuli in many cell subsets.[88,89] Together with the downregulatory effects of MXenes on CD25 and CD69 expression in total PBMCs (Figure 2C), the absence of IL-6, IFN-γ, and TNF-α (Figure 2D and Figure S4A, Supporting Information) and the concomitant decrease in LPS-induced release and expression of these cytokines (Figure 2E and Figure S4B, Supporting Information), these results suggest that V_4C_3 skew immune cells toward an anti-inflammatory phenotype also on human immune primary cells. This behavior is in line with data on Ti_3C_2 MXene reported by us and others,[25] demonstrating their bio and immune compatibility as well as their anti-inflammatory effect and the ability to reduce the production of coronavirus disease (COVID-19)-related cytokines.[14]

2.5. RNA-Sequencing Profiling of V_4C_3 MXene on PBMCs

To investigate the possible molecular mechanism of action for the immune modulation exerted by V_4C_3 MXene, we assessed the effect of the material on the gene expression of PBMCs by mRNA-seq (**Figure 6**). PBMC were treated with V_4C_3 (50 μg mL^{-1}) for 24 h or left untreated, and PBMC RNA was subjected to 3′ mRNA sequencing.

Overall, V_4C_3 induced a profound modulation of leukocyte transcriptomes (i.e., 1507 genes were differentially expressed using a stringent FDR cutoff of 0.01 (LIMMA, Figure 6A,B, list of differentially expressed genes in Table S1, Supporting Information). Ingenuity Pathway Analysis (IPA) using this list of transcripts (n = 1507) demonstrated that V_4C_3 triggered a strong upregulation of EI2F signaling (Figure 6C), with upregulation of *EIF2S1* (EIF2-α), a global suppressor of protein translation (Figure 6A,D). Immune-related pathways were strongly inhibited following V_4C_3 stimulation, as demonstrated by the negative values of the activation z-score, which predicts the direction of pathway dysregulation (activation or inhibition) based on the direction and proportion of dysregulated genes within a pathway and their mutual relationships. Immune-related pathways with an enrichment p-value of ≤ 0.01 is shown in Figure 6C, and the complete list of pathways with an enrichment p-value of ≤ 0.1 is available in Table S1 (Supporting Information). In particular, we observed a profound suppression of T helper (Th) signaling (both Th1 and Th2), interferon signaling, and downregulation of the majority of differentially expressed genes involved in antigen presentation (Figure 6C). We then proceeded to investigate more in detail specific pathways using literature curated gene-sets (see materials and methods section): CD40/CD40L pathways, T Cell Receptor (TCR) signaling, MHC1, and MHC2 pathways, Antigen Presenting Machinery (two gene sets, APM1 and APM2), and a list of IFN-γ inducible chemokines and transcription factors. For this analysis, we plotted in a heatmap the genes within these pathways with an FDR < 0.1 (Figure 6A), together with additional selected genes such as the activation marker *CD69*, and *EIF2S1* (EIF2-α), which were both downregulated following V_4C_3 incubation (Figure 6A,D). Overall, genes involved in antigen presentation, as well as MHCI and MHCII genes, and IFN-γ inducible chemokines (CXCL9, CXCL10, ad CXCL11) and transcription factors (*STAT1*, and *IRF1*), were coherently downregulated in V_4C_3 treated PBMCs.

Genes involved in TCR signaling were also dysregulated. After V_4C_3 treatment, a strong inhibition of molecular signaling downstream TCR was observed (*MAP3K8, MAPK1*, RAS/MAPK pathway; *JUN* and *FOS*, JUN/MAPK pathway), while surface markers such as *ICOS, CD247*, and *CD3DE* were upregulated, together with immune-suppressive cytokines such as *IL10*. In particular, V_4C_3 induce an inhibition of a Th in favor of a T cytotoxic polarization (downregulation of *CD4* and upregulation of *CD8A*, and IFN-γ, a marker of CD8 cytotoxic T cells). As for CD40/CD40L signaling, *CD40*, which is expressed by antigen-presenting cells, was downregulated, while CD40 ligand (*CD40LG*), which is expressed by T cells, was upregulated. The upregulation of *CD40LG*, was perhaps due to a moderate activation, in the absence of antigen stimulation, of CD8 T cells, which can transiently express CD40 ligand.[90] The mild nature of this activation is substantiated by the absence of induction of cytotoxic functions (no changes in *PRF1* and *GZMB*) and lack of upregulation of activation markers such as *IL2RA* (CD25) (Table S1, Supporting Information). However, the overexpression of *IFNG* was not consistent with the downregulation of IFN-γ inducible genes (e.g., *HLAs, CXL9, CXL10, CXCL11*). We hypothesized that the upregulation of *IFNG* transcript did not result in an increase of IFN-γ protein because of the upregulation of *EIF2S1* (EIF2-α), which is known to block IFN-γ mRNA translation into protein.[91] For this purpose, we collected the supernatant from

Figure 5. Single-cell analysis of MXene impact on human primary immune subpopulations. PBMCs were isolated from the blood of healthy donors and incubated with 50 μg mL^{-1} of Ti_3C_2 or V_4C_3 for 24 h or left untreated and stained for single-cell mass cytometry analysis. A) The tSNE analysis clusterization reports the cell subpopulations identified out of PBMCs. Cell populations were defined by manual gating strategy (Figure S5, Supporting Information), projected onto tSNE space and assigned specific colors on the basis of the signal of key phenotypic markers B) tSNE map, heatmap and histogram of cell viability analysis using cisplatin (Cis) mean values for single-cell subpopulations and total PBMCs. C) Heat maps of mean intracellular cytokine production level in gated immune cell populations for IFN-γ, IL-2, IL-4, IL-5, IL-17f, IL17a, IL-6, MIP1β, TNF-α, perforin, and GrB. Significantly up- and down-regulated cytokines ($p < 0.05$) in experimental conditions compared to negative control are highlighted with red and blue dots, respectively. All experiments were performed in triplicate and shown as means ± S.D. (one-way ANOVA and Tukey's multiple comparison test).

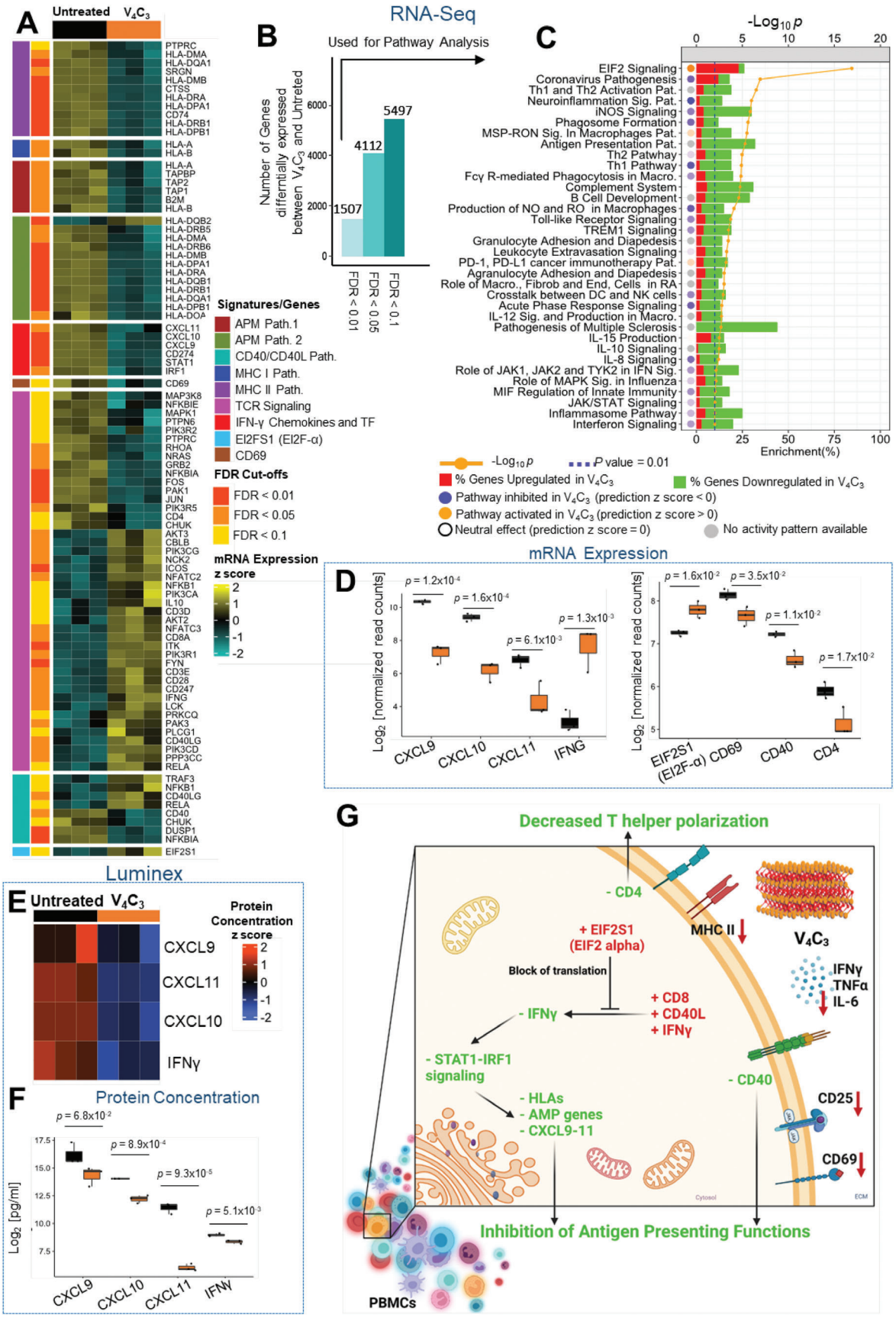

the same PBMC experiments at 24 h and measured the concentration of IFN-γ, CXCL9, CXCL10, and CXCL11 proteins by Luminex. Strikingly, the secretion of CXCL9, CXCL10, and CXCL11 decreased after V_4C_3 incubation, together with IFN-γ, confirming our hypothesis. Therefore, the inhibition of IFN-γ translation might explain the observed downregulation of IFNG inducible transcripts and proteins.

All these data are consistent and complement the results obtained by our functional assays on human primary cells for the activation marker CD69 and cytokines as well as on murine cells for CD40 and CD40L (Figures 2, 3, and 5). The RNAseq analysis conducted in this study also indicates a decrease in APM, IFN-γ, and MHC I and II signaling pathways in V_4C_3. This decrease, together with the downregulation in the gene expression of CD69, CD40, and CD4 (Figure 6D), corresponds to the reduced T helper polarization and the inhibition of the antigen-presenting functions illustrated in Figure 3C–F and Figure 2C, respectively. Furthermore, Figure 6C illustrates a decrease in the JAK/STAT signaling pathway, which is essential for T cell activation and cytokine signaling. This, along with the decrease in Th1 and Th2 pathways (Figure 6C), results in reduced macrophage activation and pro-inflammatory cytokine production, as observed in Figure 5C.

In summary, the above studies performed on cell interactions, activation status, cytokine production, and gene expression provided us with the data to depict the mechanism of V_4C_3 MXene-dependent immunosuppression (Figure 6G). The decreased Th-like polarization induced by V_4C_3, together with the downregulation of CD40, MHCI, and MHCII genes, IFN-γ transcription factors (*STAT1*, and *IRF1*), and inducible chemokines (CXCL9, CXCL10, and CXCL11) explain the V_4C_3 Mxene-dependent inhibition of the antigen presentation mechanism observed on DCs and T cells.

3. Conclusion

We have provided insights on the effects of V_4C_3, a member of the Mxene family, on immune cells and compared it to Ti_3C_2. Our observations reveal that V_4C_3 Mxene can downregulate immune functions. In particular, the material can affect the interactions between DCs and T cells, with relevance for its future use as a nanoplatform in biomedicine. By combining functional assays and a deep immune profile of V_4C_3 at the single-cell level, we fully explored the immune cell compatibility of V_4C_3 Mxene and its immune impact.

After demonstrating the hemocompatibility of the material and the absence of cytotoxicity in vitro and ex vivo toward human immune cells, we revealed its immunomodulatory activity, not dependent on cell internalization, in terms of modulation of activation markers, cytokine release, and gene expression. V_4C_3 induced a significant decrease of CD69 and CD25 activation markers in primary immune cells and strongly counteracted LPS-induced increase of key proinflammatory cytokines, often dysregulated in immunological disorders, at the protein and gene levels.

Furthermore, we demonstrated a reduction in T cell-DC interactions mediated by V_4C_3, revealing the ability of the material to completely abrogate the upregulation of CD40 and CD40L in murine $CD4^+$ T cells and dendritic cells, two key costimulatory molecules for immune activation. We then dissected the immune modulation of V_4C_3 on human primary immune cells through a phenotypical and functional profile of seventeen cell types by single-cell mass cytometry, showing that V_4C_3 skews immune cells toward an anti-inflammatory phenotype, also on human immune primary cell subpopulations. Finally, we investigated the possible molecular mechanism of action for the immune modulation exerted by V_4C_3 by mRNA-seq profiling and Luminex technology, revealing the Mxene-mediated downregulation of antigen presentation-associated genes in primary human immune cells. Having observed that only Ti_3C_2 was internalized by immune cells, while V_4C_3 was not present in any subcellular compartments, it is reasonable to speculate that the observed effects are induced by the specific chemical composition of V_4C_3 and not dependent on the material uptake. Specifically, our research has found that the presence of vanadium in the Mxene material may actually counteract V_4C_3 cell internalization. In fact, the chemistry of Mxenes could play a significant role in their uptake as suggested by well-known correlations between internalization and material chemistry.[84–86] This finding could have significant implications for the use of Mxenes in biomedical applications, as it suggests that modifications to the material's chemistry could impact its cellular uptake and potential biological effects.

In summary, our immune-profiling data suggest V_4C_3 as a promising nanoscale platform in biomedicine showing superior biocompatibility and downregulation of antigen presentation pathways compared to other vanadium-based metallodrugs reported in the literature. Further studies are needed to explore the possible application of V_4C_3, in particular as an immunomodulator and nanoagent able to induce a tolerogenic phenotype, which is a powerful immunotherapeutic strategy based on tolerogenic DCs, as recently highlighted.[38]

Figure 6. mRNA-seq profiling and Luminex protein analysis on human PBMCs. PBMCs were treated with 50 µg mL^{-1} of V_4C_3 for 24 h. A) Heatmap representing differentially expressed genes (DEGs) using Limma in V_4C_3 versus untreated (Benjamini-Hochberg FDR < 0.1) belonging to pathways of interest and selected genes (CD69 and EIF2S1). B) Histogram of number of DEGs using Limma in V_4C_3 versus untreated at different FDR cut-offs (FDR < 0.1, FDR 0.05, FDR 0.01). C) List of DEGs (FDR < 0.01) was used for pathways enrichment analysis using Ingenuity Pathway Analysis (IPA). Enriched immune-related pathways with *p* value < 0.01 and EIF2 signaling (top deregulated pathway) are shown. List of all deregulated pathways is provided in Table S1 (Supporting Information). The orange line represents the enrichment p value, the dotted blue line represents *p* value of 0.01 (−Log10 *P* value = 2). Histograms represent the proportion (%) of DEGs upregulated (red) or downregulated (green) in V_4C_3 versus untreated PBMC for each pathway. The circles represent the pathway activation score (activation z score). Blue circle indicates the pathway is inhibited, orange circle that a pathway is activated, the white circle that there is a neutral effect, while a gray circle indicates that the pathway activity is unknown (not predicted). D) Boxplot showing mRNA expression of Log2 normalized read counts for IFNG and IFNG inducible chemokines in addition to selected genes (CD40, CD4, CD69, EIF2S1) in V_4C_3 versus untreated PBMCs (Limma nominal p value is represented). Luminex analysis of PBMC supernatant from the same experiments as above. E) Heatmap and F) boxplot showing protein concentration of IFNγ and IFNγ inducible chemokines (ANOVA p value). G) Possible mechanism and effect of V_4C_3 interaction with PBMCs.

4. Experimental Section

Preparation and Characterization of Mxenes: To synthesize the MAX phase precursors, TiC (<2 µm, Alfa Aesar, 99.5%), Ti (−325 mesh, Alfa Aesar, 99.5%), Al (−325 mesh, Alfa Aesar, 99.5%), V (99.5%, −325 mesh, Alfa Aesar), and graphite (−325 mesh, Alfa Aesar, 99%) powders were utilized. For, Ti_3AlC_2, a 2:1:1 atomic ratio of TiC:Ti:Al (50 g total) was used, following prior synthesis procedures.[92] To synthesize V_4AlC_3, a 4:1.5:3 atomic ratio (10 g total) of V:Al:C was mixed. Both powder mixtures were individually mixed in a 2:1 ball:powder ratio with 5 mm alumina balls. These were then ball milled for 24 h at 60 rpm prior to high-temperature sintering. The high-temperature reactions were undertaken in a Carbolite Gero tube furnace, heating/cooling rates of 3 °C, and 200 SCCM continuous flow of ultrahigh purity Ar gas (99.999%). To produce Ti_3AlC_2, the appropriate mixture was sintered at 1400 °C for 2 h. To produce V_4AlC_3, they were instead sintered at 1500 °C for 2 h. After cooling, the porous compacts were milled using a TiN-coated milling bit and sieved (400-mesh), resulting in particles <38 µm. All experiments herein used a single batch of MAX to eliminate any batch-to-batch variation.[93]

For topochemically synthesis (selective Al etching) of Mxenes from the MAX phases, HF (Acros Organics, 48–50 wt%; 29 M), HCl (Fisher Scientific, 37 wt%; 12 M), and deionized (DI) water (15 MΩ resistivity) were used. In each reaction, PTFE stir bars were spun at 300 rpm to ensure homogeneity in the reaction. $Ti_3C_2T_x$ was produced by submerging 1 g of Ti_3AlC_2 in a 2:6:12 volumetric ratio (total of 20 mL) of HF:H_2O:HCl for 24 h at 35 °C. For $V_4C_3T_x$, 1 g of V_4AlC_3 was submerged in 20 mL of pure HF and stirred for 96 h at 35 °C. After etching, each mixture was washed with DI water by repeated centrifugation until neutral. These mixtures were added to 150 mL DI H_2O and were centrifuged at 3500 rpm for 10 min. The acidic supernatant was decanted from the sedimented Mxene. New DI H_2O was added, the multilayer Mxene sediment fully redispersed; this entire centrifugation/decantation process was repeated eight times to ensure full Mxene neutrality, with all excess adsorbed acid removed.

Both $Ti_3C_2T_x$ and $V_4C_3T_x$ were delaminated in 20 mL of 5 wt% TMAOH solution (TMAOH; Sigma Aldrich, 25 wt% in H_2O). They were stirred at 300 rpm for 12 h at 35 °C. Afterward, they were equally split into two 50 mL centrifugation tubes per Mxene. New DI H_2O was added, then the TMA-intercalated Mxenes were centrifuged for 20 min at 10 000 rpm. The clear basic supernatant was decanted, and the sedimented Mxene was then fully redispersed in new DI H_2O. This was repeated at least five times to ensure the removal of any excess TMAOH. After the last cycle, the sedimented Mxenes were redispersed in 50 mL DI H_2O, and then centrifuged for 10 min at 3,500 rpm. The supernatant was carefully decanted and collected, and then this collected supernatant was again centrifuged for 10 min at 3500 rpm. The resulting supernatant was decanted for collection and use. This extra centrifugation step ensures that all few-layer and multilayer Mxene flakes are sedimented, so that pure single-flake Mxene is collected for use in the study. A fraction of the collected solution was then vacuum filtered through Celgard membranes (64 nm pore size, 3501 coated polypropylene) to produce free-standing films for characterization, such as X-ray diffraction (XRD). Moreover, the solution concentrations were calculated by measuring the resultant film weight after drying. The synthesis of the nanomaterial was conducted under sterile conditions to prevent any potential contamination.

For material characterization, all Mxenes used in this study have been reported and characterized extensively elsewhere.[22,94] Powder and film XRD patterns were collected on a Rigaku Smartlab (40 kV and 30 mA) diffractometer using Cu K_α radiation. For the XRD pattens, the collection conditions were: i) MAX powder: a step scan of 0.02° from 3° to 90° (2θ), and 1 s step time; ii) Mxene films: a step scan of 0.03 ° from 3° to 70° (2θ) and 0.5 s step time. Scanning electron microscopy (SEM) was collected using a dual-beam focused ion beam instrument (Strata DB235, FEI). Using a porous anodic alumina substrate, a low-concentration colloidal dispersion of Mxene flakes were drop-cast. Pt was sputter-deposited to minimize charging. DLS (Zetasizer Nano ZS, Malvern Instruments) was used for flake size analysis. For each sample, three measurements were collected.

Mxenes final application was considered during their development in order to obtain a material allowing the easy preparation of biomedical formulations. The high solubility and stability of Mxenes in aqueous and polar solvents[95] allows their preparation for systemic administration. Mxene injection has been successfully performed in various animal studies, proving the biocompatibility of Mxenes (e.g., Ti_3C_2) with sizes up to 250 nm,[96–99] which is similar to the one used in this study. In addition, as reported in literature, even considering other 2D materials with lower solubility (such as graphene), the systemic injection was possible even for materials with sizes larger than 275 nm.[100] These studies suggest that our V_4C_3 with a size of ≈275 nm can be further explored for future works implying the systemic injection.

The colloidal stability of MXenes has been studied in both aqueous environments and with phosphate-buffered saline/protein solution (data not shown). After delamination, Mxenes were colloidally stable for extended periods of time with no additives, regardless of the chemistry, as previously reported.[101,102] Samples were then tested to assess their sterility (data not shown).

Hemolysis Assay: Human blood was harvested from healthy donors using ethylenediaminetetraacetic acid (EDTA) as a stabilizer. The blood samples were centrifugated at 200 × *g* for 5 min and the serum was discarded. RBCs were then washed three times with isotonic PBS. To determine the hemolytic activity, 1 mL of RBC suspension in PBS was treated with Ti_3C_2 or V_4C_3 (50 µg mL^{-1}). The mixtures were left at 37 °C in a Thermo mixer at 500/600 × *g* for 1 and 24 h. At the end of the incubation times, samples were centrifugated to remove cells, and hemoglobin absorbance in the supernatants was analyzed by a microplate reader (Sunrise TECAN Infinite M200PRO) at 570 nm, with the absorbance at 620 nm as a reference.

Isolation of Peripheral Blood Mononuclear Cells: PBMCs were isolated from EDTA-venous blood from healthy donors (25–50 years old) collected at the Transfusion Center of the University Hospital of Padua, after approval from Region of Veneto Azienda Ospedaliera di Padova (number PD5579) and individual written informed consent. A standard Ficoll-Paque (GE Healthcare, CA, USA) separation protocol was used for cell separation. Cells were cultured in 24-well plates in Roswell Park Memorial Institute (RPMI) medium (Life Technologies), additionated with 1% penicillin/streptomycin (Life Technologies) and 10% heat-inactivated fetal bovine serum (Life Technologies).

Viability and Cell Activation by Flow Cytometry: Cells were treated with different concentrations (25, 50, and 100 µg mL^{-1}) of V_4C_3 or Ti_3C_2 for 24 h and analyzed by flow cytometry (FACS Canto II, BD Bioscience, CA, USA) using the fixable Viability Stain 780 (FVS780, BD Horizon) and Annexin V (PE, BD Horizon), to evaluate cell viability and apoptosis/necrosis, respectively. Ethanol 70% as a positive control was included.

PBMC activation was evaluated after treatment with 50 µg mL^{-1} of V_4C_3 or Ti_3C_2 for 24 h. Cells were stained with antibodies specific for CD25 and CD69 activation markers (PE-conjugated anti-CD25, M-A251 clone; FITC-conjugated anti-CD69, FN50 clone; BD Bioscience, CA, USA) in the dark for 20 min. Lipopolysaccharides (LPS, 2 µg mL^{-1}; Sigma – Aldrich, Missouri, USA) was used as a positive control.

Data were acquired by flow cytometry and analyzed by FlowJo Software.

Cytokine Detection in Peripheral Blood Mononuclear Cell Supernatants: PBMCs were treated with V_4C_3 or Ti_3C_2 (50 µg mL^{-1}) in the presence or absence of LPS (2 µg mL^{-1}) priming for 24 h and the release of different cytokines (IFN-γ, IL-6, and TNF-α) was evaluated. The Cytometric Bead Array (CBA) immunoassay kit (BD Biosciences, USA) was used following the manufacturer's instructions. A BD LSR Fortessa flow cytometry system (BD Biosciences, San Jose, CA, USA) was used to acquire the data. The BD FCAP Array v3.0 software (BD Biosciences, San Jose, CA, USA) was used for data analysis. A five-parameter logistic (5-PL) equation was used to determine the standard curve. The results were based on a standard concentration curve and expressed as pg mL^{-1}.

Mxene uptake by Transmission Electron Microscopy (TEM): To perform TEM analysis, samples were fixed with 2.5% glutaraldehyde in 0.1 M sodium cacodylate buffer pH 7.4 ON at 4 °C. For postfixing, samples were treated with 1% osmium tetroxide and 1% potassium ferrocyanide in 0.1 M sodium cacodylate buffer for one hour at 4 °C. Following three washes

with water, samples were dehydrated in a graded ethanol series and embedded in an epoxy resin (Sigma-Aldrich). Using an Ultrotome V (LKB) ultramicrotome ultrathin sections (60–70 nm) were obtained, counterstained with uranyl acetate and lead citrate, and acquired with a Tecnai G2 (FEI) transmission electron microscope working at 100 kV. Images were captured using a Veleta digital camera (Olympus Soft Imaging System).

In Vitro Viability Testing on Major Immune Cell Populations Treated with Mxenes: Jurkat (T cells), JY (B cells), THP-1 (monocytes), and K562 (natural killer cells) cell lines were treated with 50 μg mL^{-1} of V_4C_3 or Ti_3C_2 for 24, and cell viability was evaluated by flow cytometry. Ethanol 70% as a positive control was used. Fixable Viability Staining Zombie NIR (Biolegend) and then analyzed by flow cytometry.

Gene Expression by Real-Time PCR: For RNA purification, cells treated as described were lysed in Triazol (500 μL, Thermo Fisher). Total RNA (500 ng) was purified, and reverse transcribed using a Triazol/RNAeasy micro kit hybrid protocol (cat# 74 004, Qiagen), followed by Omniscript reverse transcriptase (cat# 205 111, Qiagen) according to manufacturer's instructions. The RT2 SYBR green gene expression assay protocol (cat# 330 501 Qiagen) was used for the real-time PCR reactions. RT2 SYBR Green qPCR master mix and premade RT^2 qPCR Primer Assays (Qiagen) for mouse *Tnf* (cat# PPM03113G-200), *Il6* (cat# PPM03015A), and *Gapdh* (cat# PPM02946E-200) were used. Each experiment was conducted in triplicate. Gene expression analysis was computed by using the $2^{-\Delta\Delta cT}$ method with *Gapdh* as a housekeeping gene.

Mice: C57BL6/J, CD45.1 (B6.SJL Ptprca), and OT-II were maintained in our Institute. All the experiments were performed in accordance with the approved IACUC protocol number AP000001018 to Dr. Klaus Ley at the La Jolla Institute for Immunology animal facility, fully accredited by AAALAC International. The sample size was determined to be adequate based on the magnitude and consistency of measurable differences between groups. Male and female 5–12-week-old mice were used in all experiments.

Isolation of Splenic Dendritic Cells and CD4+ T Cells: To obtain dendritic cells, spleens were harvested and incubated for 30 min at 37 °C in RPMI supplemented with 2% FBS, 20×10^{-3} M HEPES, 400 U mL^{-1} type-IV collagenase (Worthington Biochemical). The samples were then disrupted to obtain single-cell suspensions. Subsequently, RBCs were lysed using ACK buffer (Lonza), and filtered through a 70 μm mesh into PBS supplemented with 0.5% BSA and 2×10^{-3} M EDTA (Phosphate buffer EDTA, PBE). DCs were isolated by magnetic cell separation (MACS) using anti-CD11c beads (Miltenyi Biotec), following the manufacturer's instructions.

To obtain Naïve CD4$^+$ T cells, spleens were handled as previously described. To isolate CD4$^+$ T cells we used the Naïve CD4$^+$ T cell isolation kit (Miltenyi Biotec) following the manufacturer's instructions.

V_4C_3 Effects on DC and T Cell Cytokines Production during Cell–Cell Interactions: We obtained DCs and CD4$^+$ T cells from mouse spleens as described above. DCs and T cells were washed three times with PBE and stained with antibodies: anti-CD4 BV421 (clone L3T4, T4 – Biolegend), anti-I-A/I-E BV421 (clone M5/114.15.2–Biolegend) and Zombie NIR fixable viability dye APC Cy7 (Biolegend). Cells were sorted using a BD FacsAria.

Sorted DCs and T cells were separately seeded into U-bottom 96-well plates. DCs and T cells were treated with Ti_3C_2 or V_4C_3 (50 μg mL^{-1}) with or w/o LPS (10 μg mL^{-1}) for 24 h.

Nonsorted cocultures of DCs and T cells (1:1) were treated with Ti_3C_2 or V_4C_3 (50 μg mL^{-1}), supplemented with 10×10^{-6} M OTII peptide ($OVA_{329\text{-}337}$) and 10 μg mL^{-1} LPS and incubated for 24 h at 37 °C. Supernatants were collected and analyzed to address cytokines production by using BD CBA Flex Sets (BD Biosciences) for mouse TNF (cat# 558 299) and IL6 (cat# 558 301) according to the manufacturer's protocol. Samples were analyzed with FACS Celesta (BD Biosciences). Data was acquired with FACSDiva software (BD Biosciences) and analyzed with FCAP array software 2.0 (BD Biosciences).

V_4C_3 effects on DCs and T Cells Gene Expression: DCs and CD4$^+$ T cells isolated and treated as described in Section 4.11 were used for the gene expression as in Section 4.8.

Mxene Modulation of CD40 and CD40L Axis: DCs and naïve CD4$^+$ T cells were isolated from CD45.1/1 and CD45.1/1 OT-II mice, respectively as described in Section 4.10. Cells (10^5 DCs and 10^5 CD4$^+$ T cells) were cocultured in U-bottom 96 well plates in the presence or absence of LPS 10 (mg mL^{-1}) and OT-II peptide (10×10^{-3} M). Samples treated with nanomaterial were exposed during the whole culture to 50 mg mL^{-1} of Ti_3C_2 or V_4C_3. After 24 h of coculture, cells were stained with antibodies specific for CD40L and CD40 and then analyzed by flow cytometry. The gating strategy excluded doublets, cell debris, and dead cells using Zombie NIR fixable viability dye APC Cy7 (Biolegend). The CD11c BV605 (clone N418 – Biolegend) and CD4 BV421 (clone RM4-5- Biolegend) markers were used to identify respectively DCs and CD4$^+$ T cells in cocultures. CD40L was identified on CD4$^+$ T cells by the presence of CD154 PE (clone MR1 – Miltenyi) on the cell surface, while CD40 on DCs by being labeled by anti-CD40 APC (clone FGK45.5 – Miltenyi).

Single-Cell Mass Cytometry (CyTOF) Analysis: PBMCs (4×10^6 cells well^{-1}) were cultured in 6-well plates and incubated with 50 μg mL^{-1} of V_4C_3 or Ti_3C_2 for 24 h. We used LPS (0.5 μg mL^{-1}; Sigma – Aldrich, Missouri, USA) and ethanol for cell biology (EtOH 70%) as positive controls. Cells were incubated with Brefeldin A (10 μg mL^{-1}; Invitrogen, CA, USA) 6 h before the end of the treatment. After incubation, cells were washed with a PBS supplemented with EDTA 0.5 M, and 5% of fetal calf serum (FCS). Cells were then combined using Cell-ID 20-Plex Pd Barcoding Kit (Fluidigm, CA, USA). Subsequently, we stained the barcoded sample with Cell-ID Cisplatin (Fluidigm, CA, USA) 1:1000, Maxpar Human Peripheral Blood Phenotyping and Human Intracellular Cytokine I Panel Kits (Fluidigm, CA, USA), following the manufacturer's instructions. To assure a uniform cell labeling with the palladium barcoding, cells were fixed and permeabilized utilizing Fix I Buffer (1X) and Barcode Perm Buffer (1×).

Subsequently, we pooled together and resuspended the samples in Maxpar Cell Staining Buffer using a 5 mL-polystyrene round-bottom tube. We then stained the cells with a cocktail of surface marker antibodies (using a 1:100 dilution for each antibody and a final volume in the tube of 800 μL) for 30 min at room temperature. We then washed the sample two times with Maxpar Cell Staining Buffer and fixed with 1 mL of 1.6% paraformaldehyde for 10 min. Following this, cells were washed twice with Maxpar Perm-S Buffer and centrifuged for 10 min at $1000 \times g$. Cells were then resuspended in 400 μL of Maxpar Perm-S Buffer and incubated for another 30 min with cytoplasmic/secreted antibody cocktail (1:100 dilution for each antibody, final volume 800 μL). Subsequently, we washed the cells two times with Maxpar Cell Staining Buffer and stained them overnight with Cell-ID Intercalator-Ir solution at the final concentration of 125×10^{-9} M. Before data acquisition, we washed the samples two times with Maxpar Cell Staining Buffer. Finally, we resuspended the samples in 2 mL of Maxpar water, and proceeded with filtration using a 0.22 μm cell strainer cap to remove possible cell clusters or aggregates. Data were analyzed using the mass cytometry platform CyTOF2 (Fluidigm Corporation, CA, USA).

Gating Strategy and Data Analysis and Visualization: The CyTOF data analysis was carried out accordingly to the methods described by Orecchioni M et al.[66,87] and Bendall et al.,[103] by using a gating strategy to exclude doublets, cell debris, and dead cells using Cell-ID Intercalator-Ir and LD. Specific PBMC subsets and subpopulations were assessed as reported in Figure S5 (Supporting Information). Normalized, background-subtracted FCS files were uploaded into Cytobank for analysis.

Cytokine data analysis was achieved using the viSNE tool. Plots showing the expression intensity of the analyzed cytokines (IFN-γ, IL-2, IL4, IL-5, IL17a, IL17f, IL6, MIP1β, TNF-α, Perforin, and GrB) and heat maps of mean marker expression ratio for all cytokines were realized.

mRNA Sequencing: In RNA extraction and QC, to evaluate the impact of V_4C_3 on PBMCs transcriptome, cells were incubated with V_4C_3 (50 μg mL^{-1}) for 24 h. Experiments were performed in triplicates on PBMCs from the same healthy donor. The supernatant was collected to measure protein concentrations (see following paragraph). Subsequently, the cell suspension was transferred into RNase-free 1.5-mL tubes, and washed two times with PBS (1 mL). Cells were then resuspended in 350 μL of RLT Buffer freshly supplemented with 1% β-mercaptoethanol and stored at −80 °C. The RNAeasy Kit (Qiagen) RNA was then used for RNA extraction following the manufacturer's instructions. RNA was quantitated on a NanoDrop (ThermoFisher) and QCed using an Agilent 2100 Bioanalyzer (Agilent, Santa Clara, California, USA). All samples had a RIN > 7.5.

In normalization and statistical analysis, mRNA-sequencing using Lexogen QuantSeq 3′ mRNA-Seq Library Prep Kit FWD for Illumina (75 single-end) with a read depth of average 8.78 M, and average read alignment of 76.12% was performed. Single samples were sequenced across four lanes, and the resulting FASTQ files were merged by sample. All FASTQ passed QC and were aligned to the reference genome GRChg38/hg19 using STAR 2.7.9a. BAM files were converted to raw counts expression matrix using *HTSeq-count*. Subsequently, "betweenLaneNormalization" normalized data (using EDAseq omitting GC and transcript length correction (not applicable for 3'mRNA-seq)) was quantiled normalization and log2 transformed (total transcript mapped to genes = 19959 genes). All downstream analysis was performed with RStudio (Version 4.1., RStudio Inc.). Differential gene expression analysis was performed between V_4C_3 and untreated with Limma via Bioconductor package "limma v. 3.50.0"[104] with Benjamini–Hochberg (B–H) FDR, using different FDR p values cut-offs (i.e., 0.01, 0.05, and 0.1). Genes were removed with rows sum equal to zero before performing Limma. Differentially expressed genes (FDR < 0.1) which belong to pathways of interest in addition to selected genes including IFN-γ and IFN-γ inducible chemokines CXCL9-11, *CD69* and *EI2FS1*, were plotted in a heatmap using Bioconductor package "ComplexHeatmap v. 2.10.0." [105] Set of genes for pathways of interest were curated from multiple resources as follows: immune pathways including Antigen Presenting Machinery (Senbabaoglu.APM1/2) and MHC I/II (Wolf.MHC.I/II_19 272 155) from Thorsson et al. 2018[106] and Sayaman et al. 2021.[107] Original names were modified to friendly names (APM Path.1/2 and MHC I/II Path) respectively. Set of genes for T-cell receptor signaling pathway (KEGG_T_CELL_RECEPTOR_SIGNALING_PATHWAY) and CD40/CD40L pathway (BIOCARTA_CD40_PATHWAY) were downloaded from Molecular Signatures Database (MsigDB), respectively: https://www.gsea-msigdb.org/gsea/msigdb/cards/KEGG_T_CELL_RECEPTOR_SIGNALING_PATHWAY, https://www.gsea-msigdb.org/gsea/msigdb/cards/BIOCARTA_CD40_PATHWAY.html. Original names were modified to TCR signaling and CD40/CD40L Path., respectively. Another set of genes include IFN-γ-inducible chemokines and key transcription factors *(CXCL9, CXCL10, CXCL11, STAT1*, and *IRF1*).

For enrichment pathway analysis, list of differentially expressed genes (V_4C_3 vs untreated, FDR < 0.01, $n = 1507$) was uploaded to Ingenuity Pathway Analysis (IPA; Ingenuity Systems, Redwood City, CA) to detect modulated pathways (IPA canonical pathways). Original pathway names can be found in Table S1 (Supporting Information), while modified "friendly names" were used in the figured. Pathway enrichment data (including upregulated/downregulated genes, activation z-score and p value) were exported from IPA and used to regenerate the IPA figure using R CRAN package "ggplot2 v. 3.3.5". Histogram and boxplots were plotted using R CRAN package "ggplot2 v. 3.3.5". Table S1 (Supporting Information) includes: gene-level raw counts, normalized Log2 gene expression matrix used for all analyses, Limma DEG analysis results, Luminex protein concentration, full list of IPA results, and gene sets with references and individual gene names.

Luminex: Supernatants from PBMCs (see previous paragraph) were collected and analyzed by Luminex technology using a Bio-Plex Pro Human Chemokine Panel. Data regarding the concentration of IFN-γ- and IFN-γ-inducible chemokines (CXCL9, CXCL10, and CXCL10) were analyzed as previously described.[24] Protein concentrations of IFNγ and IFNγ-inducible chemokines (CXCL9, CXCL10, and CXCL11) were plotted in a heatmap using "ComplexHeatmap v. 2.10.0".

Statistical Analysis: Statistical analysis for gene expression and Luminex assays is described in the previous paragraph. For all the other experiments, comparison between groups was performed by one-way ANOVA, followed by a Tukey's post hoc multiple comparison where data was normally distributed Data that did not follow the normal distribution were statistically analyzed by Kruskall-Wallis ANOVA. Two-tailed Student's t-test was performed to compare two groups. A value of $p < 0.05$ was considered significant. Sample size for all the experiments was set as $n = 3$ biological replicates if not otherwise specified. All values are expressed as mean ± S.D.

Supporting Information

Supporting Information is available from the Wiley Online Library or from the author.

Acknowledgements

L.G.D. and L.F. acknowledge the financial support from the European Union's Horizon 2020 research and innovation program under the Marie Sklodowska-Curie grant agreement No. 734381 (CARBO-IMmap). L.G.D. is thankful to the Starting Grant 2020 from the Department of Biomedical Science, University of Padua. L.G.D., Y.G., and L.F. acknowledge the funding from the European Union's Horizon 2020 research and innovation program, under the Marie Sklodowska-Curie grant agreement No. 101029140 (SEE). The authors acknowledge the funding from the European Union's Horizon Europe program, under the Marie Sklodowska-Curie grant agreement No. 101086184 (MX-MAP). SEM and XRD analyses were performed using the Materials Characterization Core instruments at Drexel University. RNA sequencing has been performed by SIDRA Medicine integrated genomic Core. Luminex assays have been performed by Sidra Medicine Deep Phenotyping Core. The work of L.F., E.A., and D.B. was also supported by Sidra Internal Funds (SDR400025).

Conflict of Interest

The authors declare no conflict of interest.

Author Contributions

L.F. and A.G. contributed equally to this work. L.G.D. conceived the project and coordinated the study. L.F., A.G., L.G.D., D.B., and Y.G. wrote the manuscript with the contribution of all authors. Y.G. coordinated the nanomaterial production and characterization. C.E.S. synthesized and characterized the materials. L.F., A.G., M.O., and E.A. performed the experiments and analyzed the data. D.B. was responsible for the gene expression analysis. L.F., A.G., M.O., K.L., D.B., and L.G.D. interpreted the experimental data with the contribution of all authors.

Data Availability Statement

The data that support the findings of this study are available from the corresponding author upon reasonable request.

Keywords

2D materials, immune system, MXene, nanomedicine, vanadium

Received: February 14, 2023
Revised: May 9, 2023
Published online: June 8, 2023

[1] A. VahidMohammadi, J. Rosen, Y. Gogotsi, *Science* **2021**, *372*, eabf1581.
[2] B. Anasori, Y. Gogotsi, *2d Mater* **2022**, *7*, 75.
[3] F. Meng, M. Seredych, C. Chen, V. Gura, S. Mikhalovsky, S. Sandeman, G. Ingavle, T. Ozulumba, L. Miao, B. Anasori, Y. Gogotsi, *ACS Nano* **2018**, *12*, 10518.
[4] E. J. Ward, J. Lacey, C. Crua, M. K. Dymond, K. Maleski, K. Hantanasirisakul, Y. Gogotsi, S. Sandeman, *Adv. Funct. Mater.* **2020**, *30*, 2000841.

[5] A. Gazzi, L. Fusco, A. Khan, D. Bedognetti, B. Zavan, F. Vitale, A. Yilmazer, L. G. Delogu, *Front. Bioeng. Biotechnol.* **2019**, *7*, 295.
[6] L. Fusco, A. Gazzi, G. Peng, Y. Shin, S. Vranic, D. Bedognetti, F. Vitale, A. Yilmazer, X. Feng, B. Fadeel, C. Casiraghi, L. G. Delogu, *Theranostics* **2020**, *10*, 5435.
[7] N. Driscoll, B. Erickson, B. B. Murphy, A. G. Richardson, G. Robbins, N. V. Apollo, G. Mentzelopoulos, T. Mathis, K. Hantanasirisakul, P. Bagga, S. E. Gullbrand, M. Sergison, R. Reddy, J. A. Wolf, H. I. Chen, T. H. Lucas, T. R. Dillingham, K. A. Davis, Y. Gogotsi, J. D. Medaglia, F. Vitale, *Sci. Transl. Med.* **2021**, *13*, eabf8629.
[8] G. P. Lim, C. F. Soon, N. L. Ma, M. Morsin, N. Nayan, M. K. Ahmad, K. S. Tee, *Environ. Res.* **2021**, *201*, 111592.
[9] H. Huang, R. Jiang, Y. Feng, H. Ouyang, N. Zhou, X. Zhang, Y. Wei, *Nanoscale* **2020**, *12*, 1325.
[10] J. Huang, Z. Li, Y. Mao, Z. Li, *Nano Select* **2021**, *2*, 1480.
[11] A. Sundaram, J. S. Ponraj, C. Wang, W. K. Peng, R. K. Manavalan, S. C. Dhanabalan, H. Zhang, J. Gaspar, *J. Mater. Chem. B* **2020**, *8*, 4990.
[12] A. Szuplewska, D. Kulpińska, A. Dybko, M. Chudy, A. M. Jastrzębska, A. Olszyna, Z. Brzózka, *Trends Biotechnol.* **2020**, *38*, 264.
[13] A. Zamhuri, G. P. Lim, N. L. Ma, K. S. Tee, C. F. Soon, *Biomed. Eng. Online* **2021**, *20*, 33.
[14] M. A. Unal, F. Bayrakdar, L. Fusco, O. Besbinar, C. E. Shuck, S. Yalcin, M. T. Erken, A. Ozkul, C. Gurcan, O. Panatli, G. Y. Summak, C. Gokce, M. Orecchioni, A. Gazzi, F. Vitale, J. Somers, E. Demir, S. S. Yildiz, H. Nazir, J.-C. Grivel, D. Bedognetti, A. Crisanti, K. C. Akcali, Y. Gogotsi, L. G. Delogu, A. Yilmazer, *Nano Today* **2021**, *38*, 101136.
[15] W. Yan, A. Rafieerad, K. N. Alagarsamy, L. R. Saleth, R. C. Arora, S. Dhingra, *Nano Today* **2023**, *48*, 101706.
[16] W. Yan, A. Rafieerad, K. Alagarsamy, L. Saleth, R. Arora, S. Dhingra, *Can. J. Cardiol.* **2022**, *38*, S107.
[17] H. Lin, X. Wang, L. Yu, Y. Chen, J. Shi, *Nano Lett.* **2017**, *17*, 384.
[18] N. Rabiee, M. Bagherzadeh, A. M. Ghadiri, Y. Fatahi, A. Aldhaher, P. Makvandi, R. Dinarvand, M. Jouyandeh, M. R. Saeb, M. Mozafari, M. Shokouhimehr, M. R. Hamblin, R. S. Varma, *ACS Appl. Biol. Mater.* **2021**, *4*, 5336.
[19] N. Rabiee, M. Bagherzadeh, M. Jouyandeh, P. Zarrintaj, M. R. Saeb, M. Mozafari, M. Shokouhimehr, R. S. Varma, *ACS Appl. Biol. Mater.* **2021**, *4*, 5106.
[20] N. Rabiee, M. Bagherzadeh, M. Heidarian Haris, A. M. Ghadiri, F. Matloubi Moghaddam, Y. Fatahi, R. Dinarvand, A. Jarahiyan, S. Ahmadi, M. Shokouhimehr, *ACS Appl. Mater. Interfaces* **2021**, *13*, 10796.
[21] B. Anasori, Y. Xie, M. Beidaghi, J. Lu, B. C. Hosler, L. Hultman, P. R. C. Kent, Y. Gogotsi, M. W. Barsoum, *ACS Nano* **2015**, *9*, 9507.
[22] M. Shekhirev, C. E. Shuck, A. Sarycheva, Y. Gogotsi, *Prog. Mater. Sci.* **2021**, *120*, 100757.
[23] K. Huang, Z. Li, J. Lin, G. Han, P. Huang, *Chem. Soc. Rev.* **2018**, *47*, 5109.
[24] L. Fusco, A. Gazzi, C. E. Shuck, M. Orecchioni, D. Alberti, S. M. D'Almeida, D. Rinchai, E. Ahmed, O. Elhanani, M. Rauner, B. Zavan, J.-C. Grivel, L. Keren, G. Pasqual, D. Bedognetti, K. Ley, Y. Gogotsi, L. G. Delogu, *Adv. Mater.* **2022**, *34*, 2205154.
[25] A. Rafieerad, W. Yan, G. L. Sequiera, N. Sareen, E. Abu-El-Rub, M. Moudgil, S. Dhingra, *Adv. Healthcare Mater.* **2019**, *8*, 1900569.
[26] A. Rafieerad, W. Yan, K. N. Alagarsamy, A. Srivastava, N. Sareen, R. C. Arora, S. Dhingra, *Adv. Funct. Mater.* **2021**, *31*, 2106786.
[27] C. Wang, S. Chen, H. Xie, S. Wei, C. Wu, L. Song, *Adv. Energy Mater.* **2019**, *9*, 1970013.
[28] Y. Zhang, J. Li, Z. Gong, J. Xie, T. Lu, L. Pan, *J. Colloid Interface Sci.* **2021**, *587*, 489.
[29] Y. Dall'Agnese, P.-L. Taberna, Y. Gogotsi, P. Simon, *J. Phys. Chem. Lett.* **2015**, *6*, 2305.
[30] Q. M. Shan, X. P. Mu, M. Alhabeb, C. E. Shuck, D. Pang, X. Zhao, X. F. Chu, Y. Wei, F. Du, G. Chen, Y. Gogotsi, Y. Gao, Y. Dall'Agnese, *Electrochem. Commun.* **2018**, 96.
[31] S.-M. Bak, R. Qiao, W. Yang, S. Lee, X. Yu, B. Anasori, H. Lee, Y. Gogotsi, X.-Q. Yang, *Adv. Energy Mater.* **2017**, *7*, 1700959.
[32] E. Lee, A. VahidMohammadi, Y. S. Yoon, M. Beidaghi, D.-J. Kim, *ACS Sens.* **2019**, *4*, 1603.
[33] W. Feng, X. Han, H. Hu, M. Chang, L. Ding, H. Xiang, Y. Chen, Y. Li, *Nat. Commun.* **2021**, *12*, 2203.
[34] H. Hu, H. Huang, L. Xia, X. Qian, W. Feng, Y. Chen, Y. Li, *Chem. Eng. J.* **2022**, *440*, 135810.
[35] A. Gazzi, L. Fusco, M. Orecchioni, S. Ferrari, G. Franzoni, J. S. Yan, M. Rieckher, G. Peng, M. A. Lucherelli, I. A. Vacchi, N. D. Q. Chau, A. Criado, A. Istif, D. Mancino, A. Dominguez, H. Eckert, E. Vázquez, T. D. Ros, P. Nicolussi, V. Palermo, B. Schumacher, G. Cuniberti, Y. Mai, C. Clementi, M. Pasquali, X. Feng, K. Kostarelos, A. Yilmazer, D. Bedognetti, B. Fadeel, et al., *J. Phys. Mater.* **2020**, *3*, 034009.
[36] W. Jiang, Y. Wang, J. A. Wargo, F. F. Lang, B. Y. S. Kim, *Nat. Nanotechnol.* **2021**, *16*, 6.
[37] Y. Mohammadzadeh, M. De Palma, *Nat. Nanotechnol.* **2022**, *17*, 442.
[38] A. Cifuentes-Rius, A. Desai, D. Yuen, A. P. R. Johnston, N. H. Voelcker, *Nat. Nanotechnol.* **2021**, *16*, 37.
[39] G. Guerrini, D. Magrì, S. Gioria, D. Medaglini, L. Calzolai, *Nat. Nanotechnol.* **2022**, 35710950.
[40] M. A. Dobrovolskaia, S. E. McNeil, *Nat. Nanotechnol.* **2007**, *2*, 469.
[41] O. Tsave, S. Petanidis, E. Kioseoglou, M. P. Yavropoulou, J. G. Yovos, D. Anestakis, A. Tsepa, A. Salifoglou, *Oxid Med Cell Longev* **2016**, *2016*, 27190573.
[42] D. Rehder, in *Interrelations between Essential Metal Ions and Human Diseases* (Eds.: A. Sigel, H. Sigel, R. K. O. Sigel), Springer Netherlands, Dordrecht **2013**, pp. 139.
[43] K. D. Mjos, C. Orvig, *Chem. Rev.* **2014**, *114*, 4540.
[44] J. J. Soldevila-Barreda, P. J. Sadler, *Curr. Opin. Chem. Biol.* **2015**, *25*, 172.
[45] D. Zamarin, *Mol. Ther.* **2018**, *26*, 9.
[46] D. Hu, D. Li, X. Liu, Z. Zhou, J. Tang, Y. Shen, *Biomed. Mater.* **2020**, *16*, 014101.
[47] W. Jiang, G. Li, W. Li, P. Wang, P. Xiu, X. Jiang, B. Liu, X. Sun, H. Jiang, *Sci. Rep.* **2018**, *8*, 9706.
[48] Y. Cao, T. Wu, K. Zhang, X. Meng, W. Dai, D. Wang, H. Dong, X. Zhang, *ACS Nano* **2019**, *13*, 1499.
[49] Y. Chen, L. Cheng, Z. Dong, Y. Chao, H. Lei, H. Zhao, J. Wang, Z. Liu, *Angew. Chem., Int. Ed.* **2017**, *56*, 12991.
[50] E. Kioseoglou, S. Petanidis, C. Gabriel, A. Salifoglou, *Coord. Chem. Rev.* **2015**, 301, *87*.
[51] A. Mravcová, D. Jírová, H. Jančí, J. Lener, *Sci. Total Environ.* **1993**, *134*, 663.
[52] P. Jiang, Q. Liu, Z. Ni, Q. Wei, X. Li, S. Xing, D. Kong, M. Li, *Regul Toxicol Pharmacol* **2018**, *94*, 1.
[53] M. M. Cunha – de Padua, S. M. Suter Correia Cadena, C. L. de Oliveira Petkowicz, G. R. Martinez, M. E. Merlin Rocha, A. L. R. Mercê, G. R. Noleto, *Carbohydr. Polym.* **2017**, *173*, 665.
[54] J. C. Pessoa, S. Etcheverry, D. Gambino, *Coord. Chem. Rev.* **2015**, *301*, 24.
[55] A. Ścibior, Ł. Pietrzyk, Z. Plewa, A. Skiba, *J Trace Elem Med Biol* **2020**, *61*, 126508.
[56] E. P. H. Chan, L. Filgueira, *Toxicol. Environ. Chem.* **2010**, *92*, 355.
[57] M. Ustarroz-Cano, I. García-Peláez, G. Piñón-Zárate, M. Herrera-Enríquez, G. Soldevila, T. I. Fortoul, *J. Immunotoxicol.* **2012**, *9*, 374.
[58] K. Lee, X. Shen, R. König, *Toxicology* **2001**, *169*, 53.
[59] Y. Gogotsi, B. Anasori, *ACS Nano* **2019**, *13*, 8491.
[60] A. Rafieerad, G. L. Sequiera, W. Yan, P. Kaur, A. Amiri, S. Dhingra, *J. Mech. Behav. Biomed. Mater.* **2020**, *101*, 103440.

[61] M. A. Hope, A. C. Forse, K. J. Griffith, M. R. Lukatskaya, M. Ghidiu, Y. Gogotsi, C. P. Grey, *Phys. Chem. Chem. Phys.* **2016**, *18*, 5099.
[62] R. Elgueta, M. J. Benson, V. C. de Vries, A. Wasiuk, Y. Guo, R. J. Noelle, *Immunol. Rev.* **2009**, *229*, 152.
[63] Y.-S. S. Yang, P. U. Atukorale, K. D. Moynihan, A. Bekdemir, K. Rakhra, L. Tang, F. Stellacci, D. J. Irvine, *Nat. Commun.* **2017**, *8*, 14069.
[64] B. Sahaf, A. Rahman, H. T. Maecker, S. C. Bendall, *Methods Mol. Biol.* **2020**, *2055*, 351.
[65] M. Anayee, N. Kurra, M. Alhabeb, M. Seredych, M. N. Hedhili, A.-H. Emwas, H. N. Alshareef, B. Anasori, Y. Gogotsi, *Chem. Commun.* **2020**, *56*, 6090.
[66] M. Orecchioni, D. Bedognetti, L. Newman, C. Fuoco, F. Spada, W. Hendrickx, F. M. Marincola, F. Sgarrella, A. F. Rodrigues, C. Ménard-Moyon, G. Cesareni, K. Kostarelos, A. Bianco, L. G. Delogu, *Nat. Commun.* **2017**, *8*, 1109.
[67] L. Fusco, E. Avitabile, V. Armuzza, M. Orecchioni, A. Istif, D. Bedognetti, T. Da Ros, L. G. Delogu, *Carbon* **2020**, *160*, 390.
[68] C. Crescio, M. Orecchioni, C. Ménard-Moyon, F. Sgarrella, P. Pippia, R. Manetti, A. Bianco, L. G. Delogu, *Nanoscale* **2014**, *6*, 9599.
[69] L. G. Delogu, E. Venturelli, R. Manetti, G. A. Pinna, C. Carru, R. Madeddu, L. Murgia, F. Sgarrella, H. Dumortier, A. Bianco, *Nanomedicine* **2012**, *7*, 231.
[70] L. G. Delogu, A. Magrini, A. Bergamaschi, N. Rosato, M. I. Dawson, N. Bottini, M. Bottini, *Bioconjug. Chem.* **2009**, *20*, 427.
[71] L. Fusco, M. Orecchioni, G. Reina, V. Bordoni, C. Fuoco, C. Gurcan, S. Guo, M. Zoccheddu, F. Collino, B. Zavan, E. Treossi, A. Yilmazer, V. Palermo, A. Bianco, L. G. Delogu, *NanoImpact* **2021**, *23*, 100330.
[72] M. Orecchioni, D. A. Jasim, M. Pescatori, R. Manetti, C. Fozza, F. Sgarrella, D. Bedognetti, A. Bianco, K. Kostarelos, L. G. Delogu, *Adv. Healthcare Mater.* **2016**, *5*, 276.
[73] M. Orecchioni, V. Bordoni, C. Fuoco, G. Reina, H. Lin, M. Zoccheddu, A. Yilmazer, B. Zavan, G. Cesareni, D. Bedognetti, A. Bianco, L. G. Delogu, *Small* **2020**, *16*, 2000123.
[74] M. Orecchioni, L. Fusco, R. Mall, V. Bordoni, C. Fuoco, D. Rinchai, S. Guo, R. Sainz, M. Zoccheddu, C. Gurcan, A. Yilmazer, B. Zavan, C. Ménard-Moyon, A. Bianco, W. Hendrickx, D. Bedognetti, L. G. Delogu, *Nanoscale* **2022**, *14*, 333.
[75] M. Pescatori, D. Bedognetti, E. Venturelli, C. Ménard-Moyon, C. Bernardini, E. Muresu, A. Piana, G. Maida, R. Manetti, F. Sgarrella, A. Bianco, L. G. Delogu, *Biomaterials* **2013**, *34*, 4395.
[76] J. Russier, V. León, M. Orecchioni, E. Hirata, P. Virdis, C. Fozza, F. Sgarrella, G. Cuniberti, M. Prato, E. Vázquez, A. Bianco, L. G. Delogu, *Angew. Chem., Int. Ed.* **2017**, *56*, 3014.
[77] R. M. Al Soubaihi, G. Furesi, K. M. Saoud, S. A. Al-Muhtaseb, A. E. Khatat, L. G. Delogu, J. Dutta, *Colloids Surf. B: Biointerfaces* **2018**, *172*, 779.
[78] A. Rozmysłowska-Wojciechowska, A. Szuplewska, T. Wojciechowski, S. Poźniak, J. Mitrzak, M. Chudy, W. Ziemkowska, L. Chlubny, A. Olszyna, A. M. Jastrzębska, *Mater. Sci. Eng., C* **2020**, *111*, 110790.
[79] K. D. Moudgil, D. Choubey, *J. Interferon Cytokine Res.* **2011**, *31*, 695.
[80] B. Fadeel, C. Bussy, S. Merino, E. Vázquez, E. Flahaut, F. Mouchet, L. Evariste, L. Gauthier, A. J. Koivisto, U. Vogel, C. Martín, L. G. Delogu, T. Buerki-Thurnherr, P. Wick, D. Beloin-Saint-Pierre, R. Hischier, M. Pelin, F. Candotto Carniel, M. Tretiach, F. Cesca, F. Benfenati, D. Scaini, L. Ballerini, K. Kostarelos, M. Prato, A. Bianco, *ACS Nano* **2018**, *12*, 10582.
[81] M. Orecchioni, D. Bedognetti, F. Sgarrella, F. M. Marincola, A. Bianco, L. G. Delogu, *J. Transl. Med.* **2014**, *12*, 138.
[82] M. Orecchioni, R. Cabizza, A. Bianco, L. G. Delogu, *Theranostics* **2015**, *5*, 710.
[83] M. Orecchioni, C. Ménard-Moyon, L. G. Delogu, A. Bianco, *Adv. Drug Delivery Rev.* **2016**, *105*, 163.
[84] H. H. Gustafson, D. Holt-Casper, D. W. Grainger, H. Ghandehari, *Nano Today* **2015**, *10*, 487.
[85] P. Sabourian, G. Yazdani, S. S. Ashraf, M. Frounchi, S. Mashayekhan, S. Kiani, A. Kakkar, *Int. J. Mol. Sci.* **2020**, *21*, 8019.
[86] Y. Qie, H. Yuan, C. A. von Roemeling, Y. Chen, X. Liu, K. D. Shih, J. A. Knight, H. W. Tun, R. E. Wharen, W. Jiang, B. Y. S. Kim, *Sci. Rep.* **2016**, *6*, 26269.
[87] M. Orecchioni, V. Bordoni, C. Fuoco, G. Reina, H. Lin, M. Zoccheddu, A. Yilmazer, B. Zavan, G. Cesareni, D. Bedognetti, A. Bianco, L. G. Delogu, *Small* **2020**, *16*, 2070117.
[88] I. Voskoboinik, J. C. Whisstock, J. A. Trapani, *Nat. Rev. Immunol.* **2015**, *15*, 388.
[89] A. C. Wensink, V. Kemp, J. Fermie, M. I. García Laorden, T. van der Poll, C. E. Hack, N. Bovenschen, *Proc. Natl. Acad. Sci. USA* **2014**, *111*, 5974.
[90] N. Q. Tay, D. C. P. Lee, Y. L. Chua, N. Prabhu, N. R. J. Gascoigne, D. M. Kemeny, *Front. Immunol.* **2017**, *8*, 1484.
[91] R. Kaempfer, *Cell Res.* **2006**, *16*, 148.
[92] C. E. Shuck, A. Sarycheva, M. Anayee, A. Levitt, Y. Zhu, S. Uzun, V. Balitskiy, V. Zahorodna, O. Gogotsi, Y. Gogotsi, *Adv. Eng. Mater.* **2020**, *22*, 1901241.
[93] C. E. Shuck, M. Han, K. Maleski, K. Hantanasirisakul, S. J. Kim, J. Choi, W. E. B. Reil, Y. Gogotsi, *ACS Appl. Nano Mater.* **2019**, *2*, 3368.
[94] A. Sarycheva, Y. Gogotsi, *Chem. Mater.* **2020**, *32*, 3480.
[95] A. Feng, Y. Yu, Y. Wang, F. Jiang, Y. Yu, L. Mi, L. Song, *Mater. Des.* **2017**, *114*, 161.
[96] Z. Liu, H. Lin, M. Zhao, C. Dai, S. Zhang, W. Peng, Y. Chen, *Theranostics* **2018**, *8*, 1648.
[97] H. Lin, S. Gao, C. Dai, Y. Chen, J. Shi, *J. Am. Chem. Soc.* **2017**, *139*, 16235.
[98] B. Sui, X. Liu, J. Sun, *J. Hazard. Mater.* **2021**, *402*, 123562.
[99] J. Wu, Y. Yu, G. Su, *Nanomaterials* **2022**, *12*, 828.
[100] H. Yue, W. Wei, Z. Yue, B. Wang, N. Luo, Y. Gao, D. Ma, G. Ma, Z. Su, *Biomaterials* **2012**, *33*, 4013.
[101] K. Maleski, C. E. Shuck, A. T. Fafarman, Y. Gogotsi, *Adv. Opt. Mater.* **2021**, *9*, 2001563.
[102] M. Seredych, K. Maleski, T. Mathis, Y. Gogotsi, *Colloids Surf. A* **2022**, *641*, 128580.
[103] S. C. Bendall, E. F. Simonds, P. Qiu, E. D. Amir, P. O. Krutzik, R. Finck, R. V. Bruggner, R. Melamed, A. Trejo, O. I. Ornatsky, R. S. Balderas, S. K. Plevritis, K. Sachs, D. Pe'er, S. D. Tanner, G. P. Nolan, *Science* **2011**, *332*, 687.
[104] M. E. Ritchie, B. Phipson, D. Wu, Y. Hu, C. W. Law, W. Shi, G. K. Smyth, *Nucleic Acids Res.* **2015**, *43*, e47.
[105] Z. Gu, R. Eils, M. Schlesner, *Bioinformatics* **2016**, *32*, 2847.
[106] V. Thorsson, D. L. Gibbs, S. D. Brown, D. Wolf, D. S. Bortone, T.-H. Ou Yang, E. Porta-Pardo, G. F. Gao, C. L. Plaisier, J. A. Eddy, E. Ziv, A. C. Culhane, E. O. Paull, I. K. A. Sivakumar, A. J. Gentles, R. Malhotra, F. Farshidfar, A. Colaprico, J. S. Parker, L. E. Mose, N. S. Vo, J. Liu, Y. Liu, J. Rader, V. Dhankani, S. M. Reynolds, R. Bowlby, A. Califano, A. D. Cherniack, D. Anastassiou, et al., *Immunity* **2018**, *48*, 812.
[107] R. W. Sayaman, M. Saad, V. Thorsson, D. Hu, W. Hendrickx, J. Roelands, E. Porta-Pardo, Y. Mokrab, F. Farshidfar, T. Kirchhoff, R. F. Sweis, O. F. Bathe, C. Heimann, M. J. Campbell, C. Stretch, S. Huntsman, R. E. Graff, N. Syed, L. Radvanyi, S. Shelley, D. Wolf, F. M. Marincola, M. Ceccarelli, J. Galon, E. Ziv, D. Bedognetti, *Immunity* **2021**, *54*, 367.

